

NANOscientific

VOL 21 WINTER 2021

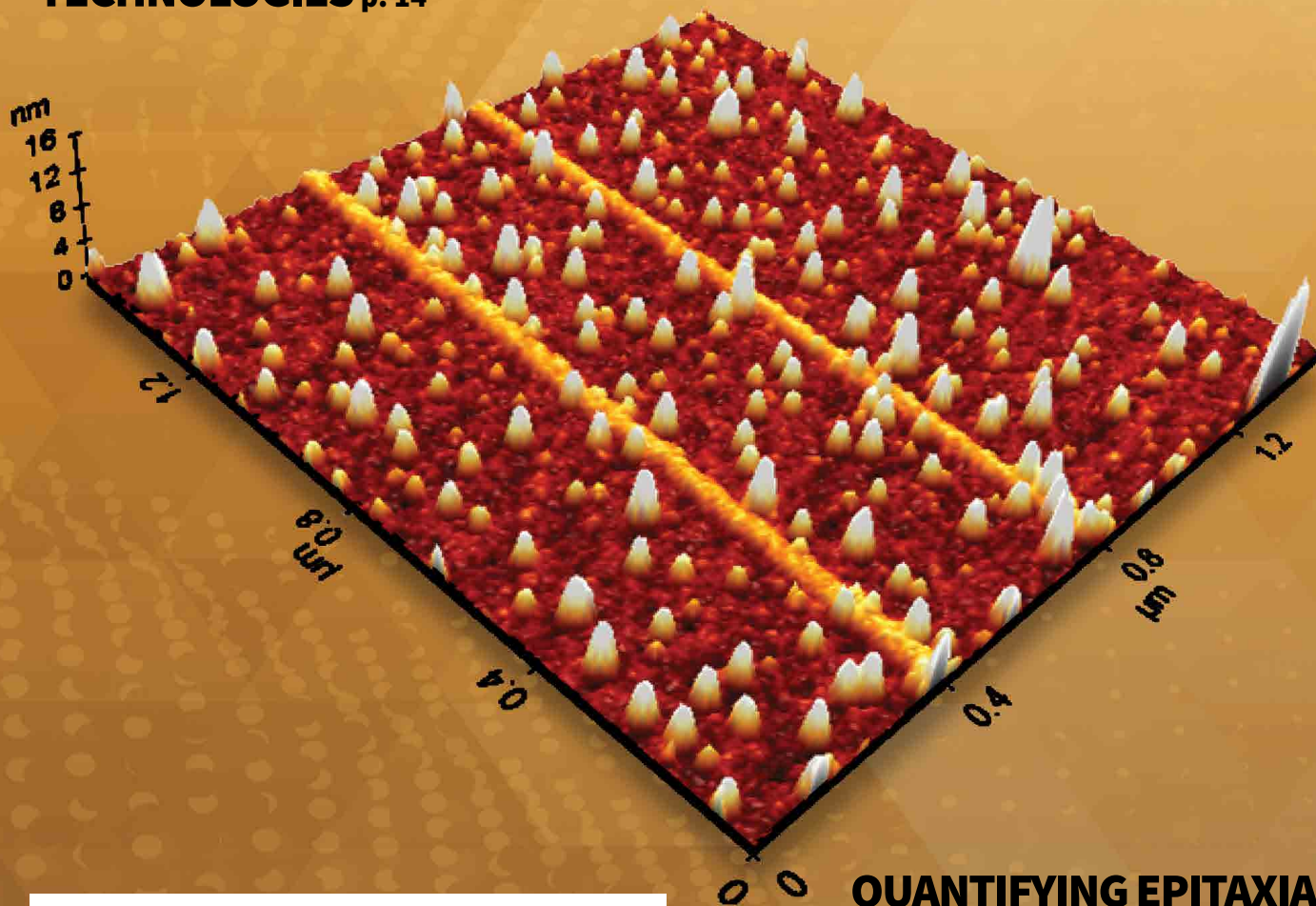
The Magazine for NanoScience and Technology

**MAGNETIC NANOSCAVENGERS:
THE NEW TREND TO IMPROVE
WATER QUALITY** p. 4

**CONTACT AFM
NANOLITHOGRAPHY BASED
ON ANODIC OXIDATION** p. 7

**APPLICATION-SPECIFIC
CHARACTERIZATIONS AND
ANALYSES OF CARBON-
BASED MATERIALS UTILIZING
DIFFERENT MICROSCOPIC
TECHNOLOGIES** p. 14

**IMPROVED ELECTRICAL
CHARACTERIZATION OF
ADVANCED MATERIALS
IN HIGH VACUUM
ENVIRONMENT** p. 17



**QUANTIFYING EPITAXIAL
GROWTH USING A PURELY
TOPOGRAPHICAL SIGNAL** p. 19

**A COMPARATIVE STUDY OF
ATOMIC FORCE MICROSCOPY** p. 25

TABLE OF CONTENTS

NanoScientific Vol 21

Magnetic Nanoscavengers: The New Trend to Improve Water Quality

Santiago, Estephany

Contact AFM Nanolithography Based on Anodic Oxidation

Park Systems Technical Services

High resolution imaging of single PTFE molecules on Teflon surface

Vladimir Korolkov, Park Systems UK

Application-specific characterizations and analyses of carbon-based materials utilizing different microscopic technologies

Manjov Aravind

Improved Electrical Characterization of Advanced Materials in High Vacuum Environment

John Paul Pineda, Charles Kim, and Byong Kim Park Systems Inc., Santa Clara, CA USA

Quantifying Epitaxial Growth using a Purely Topographical Signal

Kai Trepka

A Comparative Study of Atomic Force Microscopy between AM-KPFM and Sideband KPFM

Principles and Applications, Research Application Technology Center, Park Systems Corporation

4

7

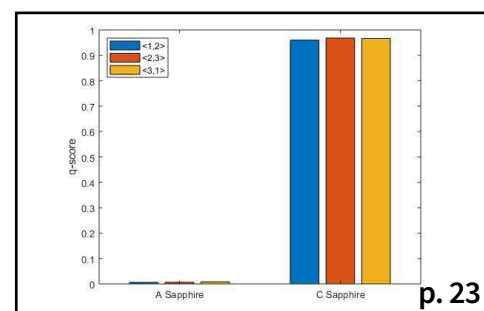
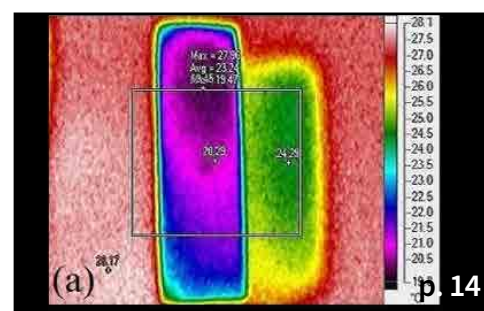
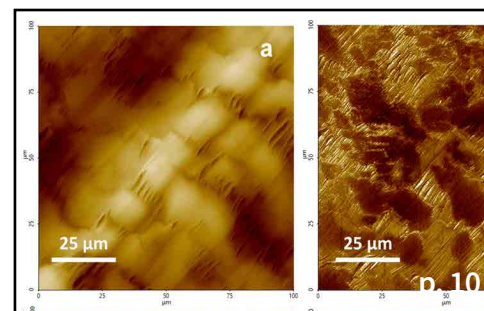
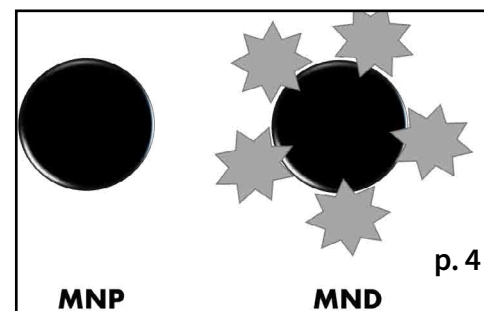
10

14

17

19

25



MESSAGE FROM EDITOR

Welcome to the 21st edition of NanoScientific. As we look into the beginning of a new year, NanoScientific has a few surprises coming out. First, we will introduce NanoScientific TV, compelling interviews and videos of the leading-edge nano researchers, a sneak peek into nanotechnology of tomorrow. We will also introduce NanoScientific App, which will give you easier access to submit abstracts, read articles online and network with others using the new NS Community Forum.

We have published articles in this issue from four of our young presenters at NanoScientific Symposium for a Changing World, including Winner of “The Most Promising Future Application Award” at the Poster Exhibition, Estephany Santiago, with her article Magnetic Nanoscavengers: The New Trend To Improve Water Quality and a short Q&A from her below. Congratulations for all of our winners at NSCW, Best Poster – Lynn Krushinski; Committee Choice – Cody Leasor; Most Promising Future Application – Estephany Santiago; Committee Choice – Hang Ran; Microscopy Award – Myunghoon Choi; Best Presentation – Louis Rogowski; Most Promising Future Application – Piran Kidambi and to all the presenters who gave inspiring talks about future research that will improve our world. In this issue, you will find four of these presenters’ articles with research leading to new approaches in understanding nanoscience which were presented at the Virtual NanoScientific Symposium. Next year, in 2021, we are planning many more virtual NanoScientific Symposiums with an in person option, if possible.

Stay tuned for dates of these events.

I am also proud to announce a new member to the NanoScientific Board, Marine Le Bourer, CEO of NanoTechnology World Association. Marine has been a huge collaborator with NanoScientific for several years and we are glad to have her as an official member of the board.

We pledge to continue to bring you exciting articles and symposiums that highlight the best of the most creative scientific minds of our time, who collectively are elevating nanotechnology to great new heights. We applaud the intensity and dedication that nano researchers put into the effort to unravel the mysteries of science one atom at a time. It is our honor to report on their achievements.

Stay safe during the New Year and may you have a very prosperous and rewarding year to come.

Keibock Lee
Editor-in-Chief



Q&A with Estephany Santiago, winner “Most Promising Future Application” Poster at NanoScientific Symposium for a Changing World

What was it like to receive the NanoScientific Most Promising Future Application Award?

It was an honor and a pleasant surprise that my research can be considered for a promising application gives me the motivation to keep working towards new applications.

Did you enjoy the NanoScientific Symposium and would you recommend it to others?

NANOScientific 2020 EDITORIAL BOARD



Dr. Rigoberto Advincula, Professor, Department of Macromolecular Science and Engineering at Case Western Reserve University.



Dr. Lane Baker, James L. Jackson Professor of Chemistry Indiana University



Mr. Phil Kaszuba, Global Foundries Senior Member of Technical Staff and lead engineer in their Scanning Probe Microscopy (SPM) laboratory.



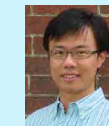
Dr. John A. Marohn, Professor & Director of Undergraduate Studies, Department of Chemistry and Chemical Biology Member, Field of Materials Science & Engineering, Cornell University.



Dr. Ye Tao, Rowland Fellow & Principle Investigator, Rowland Institute of Science at Harvard University, BA Harvard in Biochemistry, PhD MIT/ETH Zurich Chemistry



Dr. Gwo-Ching Wang, Travelstead Institute Chair, Dept. of Physics, Applied Physics & Astronomy, Rensselaer Polytechnic Institute.



Dr. Jiahua Jack Zhu, PhD, University of Akron, Associate Professor, Department of Chemical and Biomolecular Engineering.



Dr. Yiping Zhao, Professor, Department of Physics and Astronomy, Director, Nanoscale Science and Engineering Center, The University of Georgia.



Marine Le Bourer, Founder, The Nanotechnology World Association (NWA), created to help accelerate the integration of nanotechnologies in various industries.

The NanoScientific symposium is a great symposium, the best online experience that I had until now, very well organized with a great interactive website and with great presentations/posters. I will recommend all my colleagues and friends to join the upcoming symposiums.

What is your hope for your research to expand so it can be offered to clean water across the world?

My hope is that governments and private companies are encouraged to use new environmentally-friendly alternatives and invest in projects like this to take advantage of water and its reuse. It is urgent and mandatory that we focus on treating and reusing the water we throw away, to reduce our environmental impact and help the most needed communities.

NANOScientific

Keibock Lee, Editor-in-Chief
kei@nanoscientific.org

Debbie West, Content Editor
debbiewest@nanoscientific.org

Byong Kim, Technical Director

Debbie Bishop, Art Director

Elizabeth Martinez - Digital & Promotions

Sonia Lee - User Experience & Virtual Symposiums

Publisher & Corporate Officers
Park Systems Corporation

Sang-il Park, Chief Executive Officer

Karen Cho, VP of Finance
Keibock Lee, President

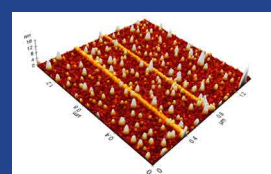
NANOScientific is published quarterly to showcase advancements in the field of nanoscience and technology across a wide range of multidisciplinary areas of research. The publication is offered free to anyone who works in the field of nanotechnology, nanoscience, microscopy and other related fields of study and manufacturing.

We enjoy hearing from you, our readers. Send your research or story ideas to debbiewest@nanoscientific.org

To view all of our articles, please visit our web site at www.nanoscientific.org

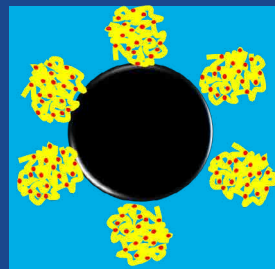
INSET PHOTO ON COVER:

Park AFM's nanolithography is an advanced AFM technique used to pattern nanoscale shapes on the sample surface. A bias voltage is applied to the tip to generate an oxide pattern on a metallic or semiconductor substrate in the bias-assisted or anodic oxidation method. The 3D image of oxide patterns formed through Park AFM nanolithography shows the types of nanometer-sized structures that can be fabricated with angstrom level scanning precision using SmartScan™ Nanolithography of Park NX10 AFM system.



Park SYSTEMS

Park Systems, Inc.
3040 Olcott Street,
Santa Clara, CA 95054
inquiry@parksystems.com
www.parksystems.com



MAGNETIC NANOSCAVENGERS: THE NEW TREND TO IMPROVE WATER QUALITY

Estephany Santiago^a, Georgina Pina-Luisa, Marisel^a Martínez-Quiroz^b, Oscar Perez-Landeros^c, Navor Rosas-González^c, Benjamin Valdez-Salasc, Mercedes T. Oropeza-Guzmán^a

^a Tecnológico Nacional de México/Instituto Tecnológico de Tijuana, Centro de Graduados de Investigación en Química, Tijuana, B.C., MX

^b CETYS Universidad, Centro de Innovación y Diseño, Av. CETYS Universidad No. 4 Fracc. El Lago, Tijuana, B.C. CP 22210, MX

^c Universidad Autónoma de Baja California, Campus Mexicali, Instituto de Ingeniería, Mexicali, B.C. MX

Tecnológico Nacional de México/Instituto Tecnológico de Tijuana, Posgrado en Ciencias de la Ingeniería, Blvd. Alberto Limón Padilla s/n, Col. Otoy, Tijuana, B.C. 22500 MX.

Introduction

Reusing water is mandatory in regions where water scarcity is due to climatic conditions, but also it offers the opportunity to mitigate water pollution by reducing the discharge of wastewater to natural surface waters.[1,2] The challenge is to develop sustainable processes to recover clean water from wastewater avoiding the use of non-degradable materials (synthetic polymers and resins), keeping low energy consumption and diminishing the investment cost to operate the technology. Water conditioning technologies such as inverse osmosis, chemical precipitation, ion exchange, and electrochemical removal, are generally used to improve water quality and aesthetics (such as alkalinity and hardness) after primary and secondary processes.[3,4] However, all of them are onerous and require meticulous maintenance to keep efficient operations and improve water quality.[3,5,6] In this pathway, we propose for the first time, the use of magnetic nanoscauengers with high potential to remove hardness and alkalinity from reclaimed water (RW). With this innovation we look to increase the water potential reuse in a simple magnetic contact stage to trap salts.

In this paper three types of eco-friendly magnetic nanoparticles were prepared using chitosan, nanodiamond powder, and grafted chitosan. All of them were coupled with magnetite nanoparticles to obtain magnetic chitosan (MCH), magnetic nanodiamond (MND), and magnetic carbamoyl chitosan (MCCH). All the materials were characterized, previous their use, by FT-IR, STEM, Zeta Potential, DLS, and TGA studies, proving

the binding between magnetite and the modifiers. Furthermore, RW in contact with magnetic nanoscauengers was used as a model to evaluate their alkalinity and hardness removal capacity. We found out that each magnetic nanoscauenger proved to be effective for trapping and removing alkaline carbonates from reclaimed water, and we demonstrated it by different techniques. At the same time, we have the possibility of recovering them for further use, reducing the operation cost. Resulting residues are not at all toxics and do not require special handling. With all these characteristics we can classify the magnetic nanoscauengers as sustainable nanomaterials.

Experimental

Low molecular weight chitosan and nanodiamond powder were used as obtained from the suppliers, Carbamoyl Chitosan was prepared with the methodology reported by Martínez-Quiroz et al. [7] Magnetic nanoparticles and Magnetic nanoscauengers (MCH, MND, MCCH) were synthesized via chemical co-precipitation under alkaline condition inspired in the methodology reported by Liu et al[8] with slight modifications. All the materials were characterized by SEM/STEM (Tescan Lyra 3GM), FT-IR (Shimadzu FT-IR Spirit ATR mode), TGA (Perkin Elmer equipment TGA 4000, DLS and Z potential (Anton Paar Litesizer 500) RW samples were taken from the wastewater treatment plant "La Morita" (Tijuana, México). With those samples we prove magnetic nanoscauengers effectiveness to remove alkalinity and hardness.

The RW was treated with the four magnetic nanoscauenger to study the

improvement of the water quality in terms of alkalinity and hardness removal. This study was performed at pH 7, 8, and 9. A dosage of 30 mg per liter of water of magnetic nanoscauenger (MNP, MND, MCH, MCCH) was weighed and then placed into the RW sample at the pH previously adjusted. The solution was sonicated for 5 minutes and then placed into an orbital shaker for 10 minutes at 360 rpm. After this time, the nanoparticles were recovered by magnetic decantation. Alkalinity and hardness were measured with standard methods for that purpose.

Results and discussion

RW original characteristics are shown in table I. Special attention is posed on alkalinity and hardness, since these parameters are among those that need to be improved to increase water potential reuse. The first strategy was done measuring the Zeta potential of raw RW, as well as the hydrodynamic diameter of residual suspended particles, for further comparison with Zeta potential of magnetic nanoscauengers dispersions. Figure 1 illustrates the nanometric conception of magnetic nanoparticle with the three different types of nanostructures. These molecular assemblies were obtained by the coprecipitation method and its stability was tested by several techniques. Figure 2. shows the physical and chemical properties of magnetic nanoscauengers by FT-IR, TGA, Zeta Potential, DLS and STEM, proving the suitable binding between magnetite and the modifiers.

Among the magnetic nanoscauengers (MND, MCH and MCCH) the surface

chemistry can be related to its physical aspect. For example, particle size vs. Zeta potential suggests that MCCH is composed of very thin particles that has an acid-base performance. Later on SEM images show the low agglomeration level due to the carbamoyl benzoic acid incorporated to the magnetic nanoparticle. In contrast MCH shows larger particles and also a completely opposite DLS profile.

Figure 3a. corresponds to the Zeta potential and DLS practiced to RW, showing low Zeta potential values at pH<4 and negative values reaching -14 mV at pH 10. This result is certainly due to water content. In contrast DLS shows larger particles at greater pH suggesting some salts precipitation when diminishing proton concentration. In Figure 3b a bar graph shows the alkalinity and hardness of RW at three different pH values that will serve to estimate the percentage of alkalinity and hardness removal when magnetic nanoscauenger are in direct contact with RW.

Figure 4. allow to evaluate the action of magnetic nanoscauengers by the hydrodynamic diameter and Zeta potential. These techniques are commonly used to characterize colloidal nanoparticles; and in this study both of them demonstrated to be important tools to evaluate water quality before and after a conditioning process. Figure 5. corresponds to the final result of alkalinity and hardness removal at three different pH for the four magnetic nanoscauengers. Concerning MCH and MCCH they showed to be the most performant for hardness removal. In the case of alkalinity MCH and MCCH are doing the same effect at pH 9. MCH showed to be the more performant nanoscauenger, in particular at pH 8, that is the closest value to the raw RW.

Conclusions

Thanks to the chemical modification of magnetite, it was possible to obtain three different magnetic nanomaterials (MND, MCH, and MCCH) which act as magnetic nano-softeners. We found out that each magnetic nanoscauenger proved to be effective for trapping and removing carbonates from reclaimed water, and we demonstrated it by different techniques. At the same time, we have the possibility of recovering magnetic nanoscauengers for further use and reduce the operation cost. With all these characteristics we can classify the prepared materials as sustainable nanomaterials.

Parameter	Reclaimed Water	Cations in Reclaimed Water	Units [ppm]	Anions in Reclaimed Water	Units [ppm]
Turbidity (NTU)	23	Li ⁺	0	F ⁻	0
pH	8	Na ⁺	287.59	Cl ⁻	378.55
Color (HU)	253	K ⁺	33.95	NO ₂ ⁻	4.30
Total suspended solids (mg L ⁻¹)	15.3	Ca ²⁺	57.37	Br ⁻	0
Particle size (nm)	566.9	Mg ²⁺	126.64	NO ₃ ⁻	117.41
Zeta Potential	-7.59			SO ₄ ²⁻	383.55
Chemical Oxygen demand (mg L ⁻¹)	74.0				
Total Organic Carbon (mg L ⁻¹)	19.4				
Electrical conductance (mS cm ⁻¹)	2.8				

Table I. Composition of reclaimed water obtained from the wastewater plant treatment "La Morita" in Tijuana, Baja California, México.

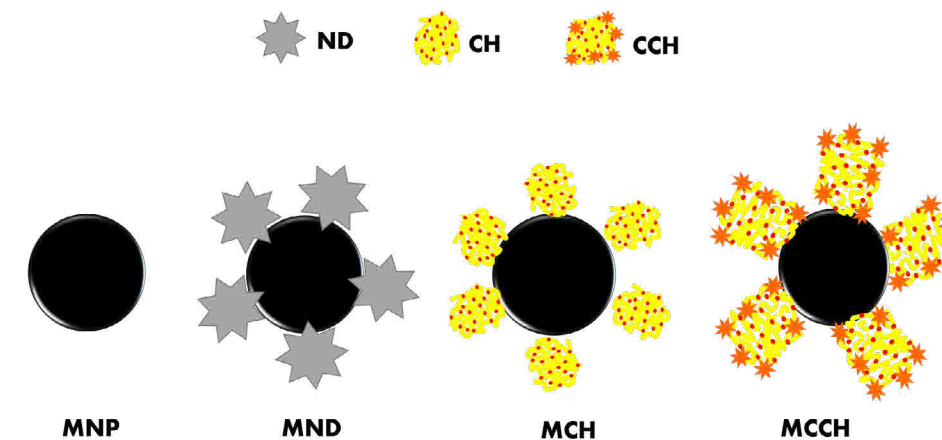


Figure 1. Schematic illustration of the formation of the nanoscauengers MND, MCH, and MCCH.

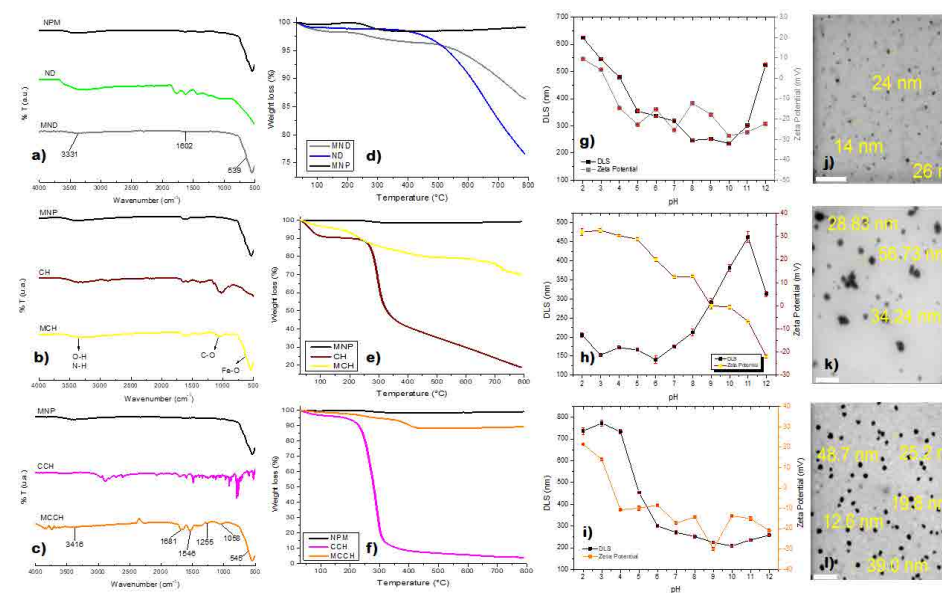


Figure 2. Characterization of Magnetic nanoscauengers by: FT-IR: a) MND, b) MCH c) MCCH; TGA: d) MND, e) MCH, f) MCCH; DLS/Zeta Potential vs pH: g) MND, h) MCH, i) MCCH; and STEM: j) MND, k) MCH, l) MCCH. The white line represents a scale bar of 200 nm.

Biographies



Estephany Santiago is a Ph.D. student in chemistry sciences at Tecnológico Nacional de México (TecNM) Campus

Tijuana (Mex) where she is performing new technological developments in the use of magnetic nanoparticles for water treatments. She began to study in Tijuana in 2014 and she obtained her M.S. in chemistry in 2016 where she developed nanostructured polymeric beads for controlled drug delivery. From 2016 to 2018 she worked as a teacher at middle school and high school level as well at the TecNM campus Tuxtla Gutiérrez in the department of chemical and biochemical engineering. In 2013 she started to work as an epidemiology assistant at the Health Department of the state of Chiapas, Mexico. She received her B.S. in Chemical Engineering from TecNM campus Tuxtla Gutiérrez in 2012 where she designed a photobioreactor for the culture of microalgae for bio-oil production.



Mercedes T. Oropeza-Guzmán is professor of Ph. D. and M. Sc. Engineering programs at Tecnológico Nacional

de México (TecNM) Campus Tijuana (Mex). Her expertise is Electrochemistry, Environmental Engineering and Nanotechnology. She is interested in all physicochemical processes related with soil and water decontamination, as well as the design of new materials for food, health, energy, and environmental applications. She has advised more than 20 Ph.D. and M.Sc. thesis dealing with electrochemical processes serving to treat water and soil. In the last three years she is author and co-author of 25 JCR papers, and she is currently in charge of enterprise partnerships with her academic institution.

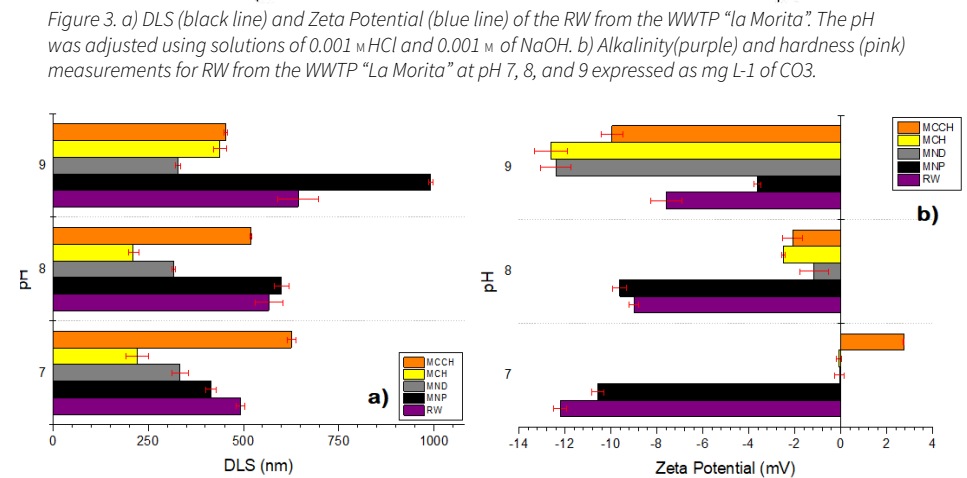
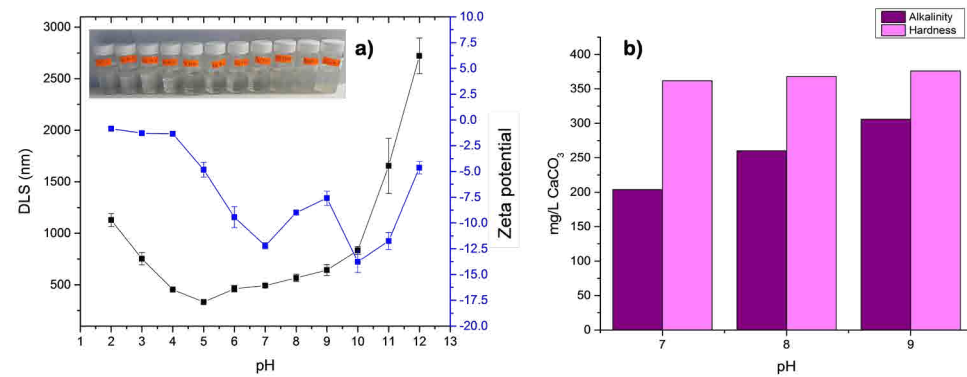


Figure 4. DLS measurements of untreated RW (purple), and RW treated with MNP (black), MND (gray), MCH (yellow), and MCCH (orange) at pH of 7, 8, and 9. d) Comparison of the Zeta Potential measurements of untreated RW (purple), and treated with MNP (black), MND (gray), MCH (yellow), and MCCH (orange) at pH of 7, 8, and 9.

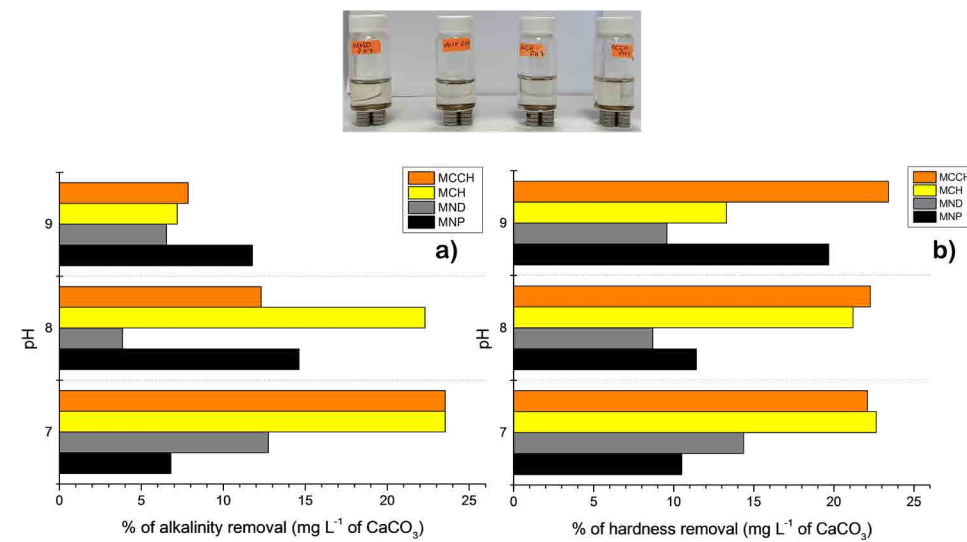


Figure 5. a) Comparison of the alkalinity removal of MNP (black), MND (gray), MCH (yellow), and MCCH (orange). b) Comparison of the hardness removal of MNP (black), MND (gray), MCH (yellow), and MCCH (orange). At pH of 7, 8, and 9, expressed as percentage in mg L⁻¹ of CaCO₃.

References

- [1] Escalante Estrada, V. E. Reúso Del Agua Residual En México, Curso inte.; Instituto Mexicano de Tecnología del Agua: Morelos: Morelos, México, 2004.
- [2] THE WORLD BANK. Water Resources and Environment Technical Note F.3; DAVIS, R., HIRJI, R., Eds.; The International Bank for Reconstruction and Development/THE WORLD BANK, 2003.
- [3] Crittenden, J. C.; Trussell, R. R.; Hand, D. W.; Howe, K. J.; Tchobanoglous, G. MWH's Water Treatment: Principles and Design; John Wiley & Sons, 2012.
- [4] Fu, F.; Wang, Q. Removal of Heavy Metal Ions from Wastewaters: A Review. J. Environ. Manage. 2011, 92 (3), 407–418.
- [5] Rajasulochana, P.; Preethy, V. Comparison on Efficiency of Various Techniques in Treatment of Waste and Sewage Water – A Comprehensive Review. Resour. Technol. 2016, 2 (4), 175–184.
- [6] Mahamuni, N. N.; Adewuyi, Y. G. Advanced Oxidation Processes (AOPs) Involving Ultrasound for Waste Water Treatment: A Review with Emphasis on Cost Estimation. Ultrason. Sonochem. 2010, 17 (6), 990–1003.
- [7] Martínez-Quiroz, M.; López-Maldonado, E. A.; Ochoa-Terán, A.; Pina-Luis, G. E.; Oropeza-Guzmán, M. T. Modification of Chitosan with Carbamoyl Benzoic Acids for Testing Its Coagulant-Flocculant and Binding Capacities in Removal of Metallic Ions Typically Contained in Plating Wastewater. Chem. Eng. J. 2018, 332, 749–756.
- [8] Liu, X.; Ma, Z.; Xing, J.; Liu, H. Preparation and Characterization of Amino-Silane Modified Superparamagnetic Silica Nanospheres. J. Magn. Magn. Mater. 2004, 270 (1), 1–6.

APPLICATION NOTE

CONTACT AFM NANOLITHOGRAPHY BASED ON ANODIC OXIDATION

Park SYSTEMS

Armando Melgarejo, Ben Schoenek, Jiali Zhang, and Byong Kim
Park Systems, Inc., Santa Clara, CA, USA

Introduction

The field of nanotechnology has diversified into different areas of research, from materials science to biotechnology. Many of these applications are based on the capability to fabricate or manipulate nanostructured materials [1]. One convenient technique for structuring, manipulation, and fabrication at the nanometer scale is atomic force microscopy (AFM) nanolithography. All AFM nanolithography techniques can be classified into two general groups in terms of their operational principles: force-assisted and bias-assisted nanolithography [2]. The force-assisted method consists of applying a large force

to a sharp tip to mechanically modify the surface atoms or molecules of the sample and produce trenches on the surface. In this case, the interaction between the tip and the sample is purely mechanical [2]. On the contrary, the bias-assisted method entails applying a voltage between the AFM tip and the substrate in contact with the sample. The tip-sample voltage induces an electrochemical reaction that produces oxide on the surface of the substrate [1].

This application note demonstrates an electrochemical process called anodic oxidation using the bias-assisted lithography method to create oxide

patterns on the surface of a silicon substrate. The success of this technique relies on using the AFM tip as a biased cathode to the sample surface. Also, the water meniscus around the sample acts as an electrolyte for the chemical reaction. The environment humidity directly influences the size of the meniscus [1]. Therefore, this application shows nanoscale oxide line formation using AFM anodized lithography on a Park NX10 AFM system using Park SmartLitho, the new nanolithography software developed by Park Systems. Park SmartLitho [3] can also be used for nanomanipulation, scratching techniques, and high voltage lithography.

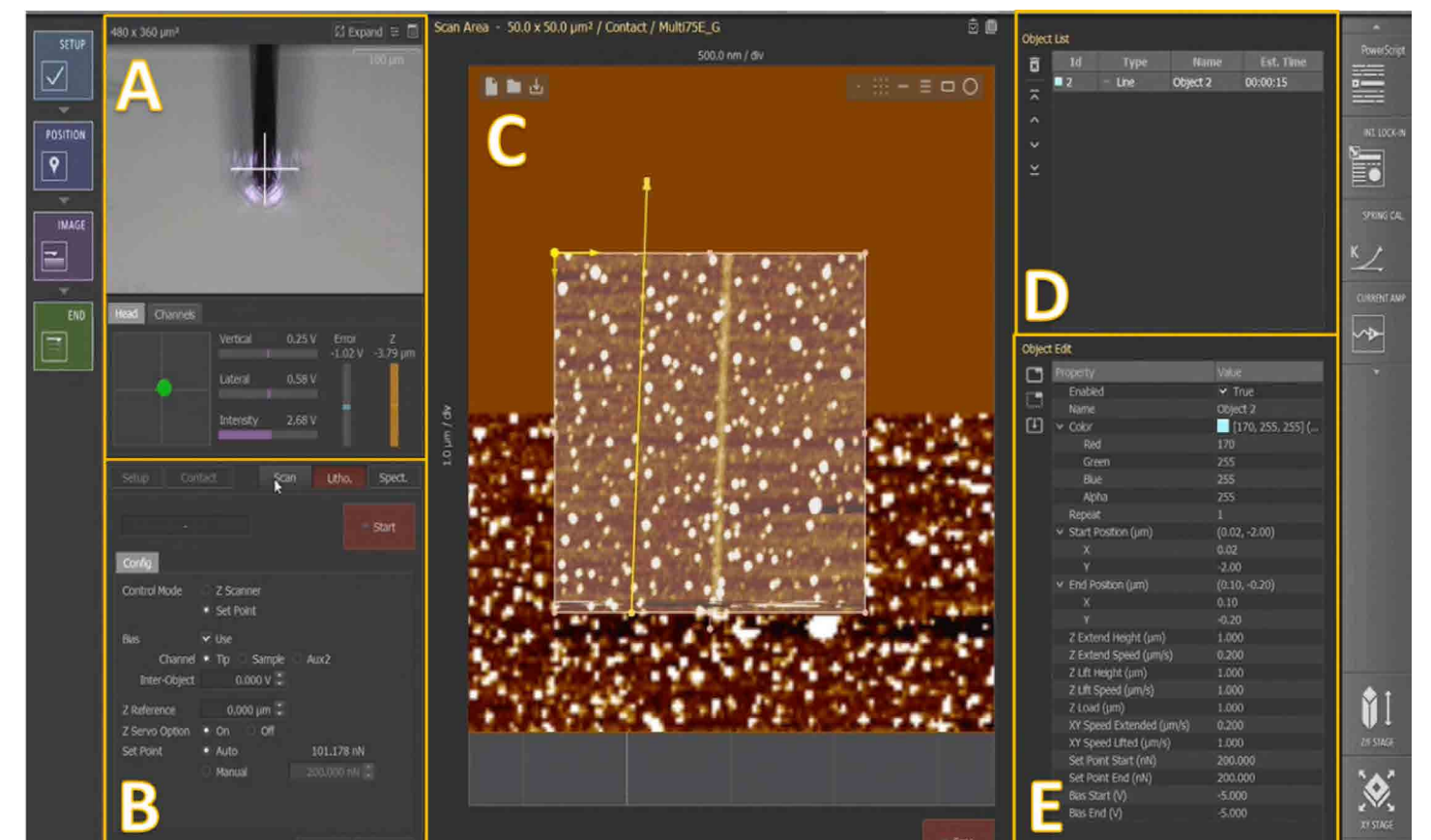


Figure 1. Park SmartLitho™ software. A) Vision & Monitoring view. B) Nanolithography mode panel. C) Lithography design area. D) Object list. E) Objects edit panel.

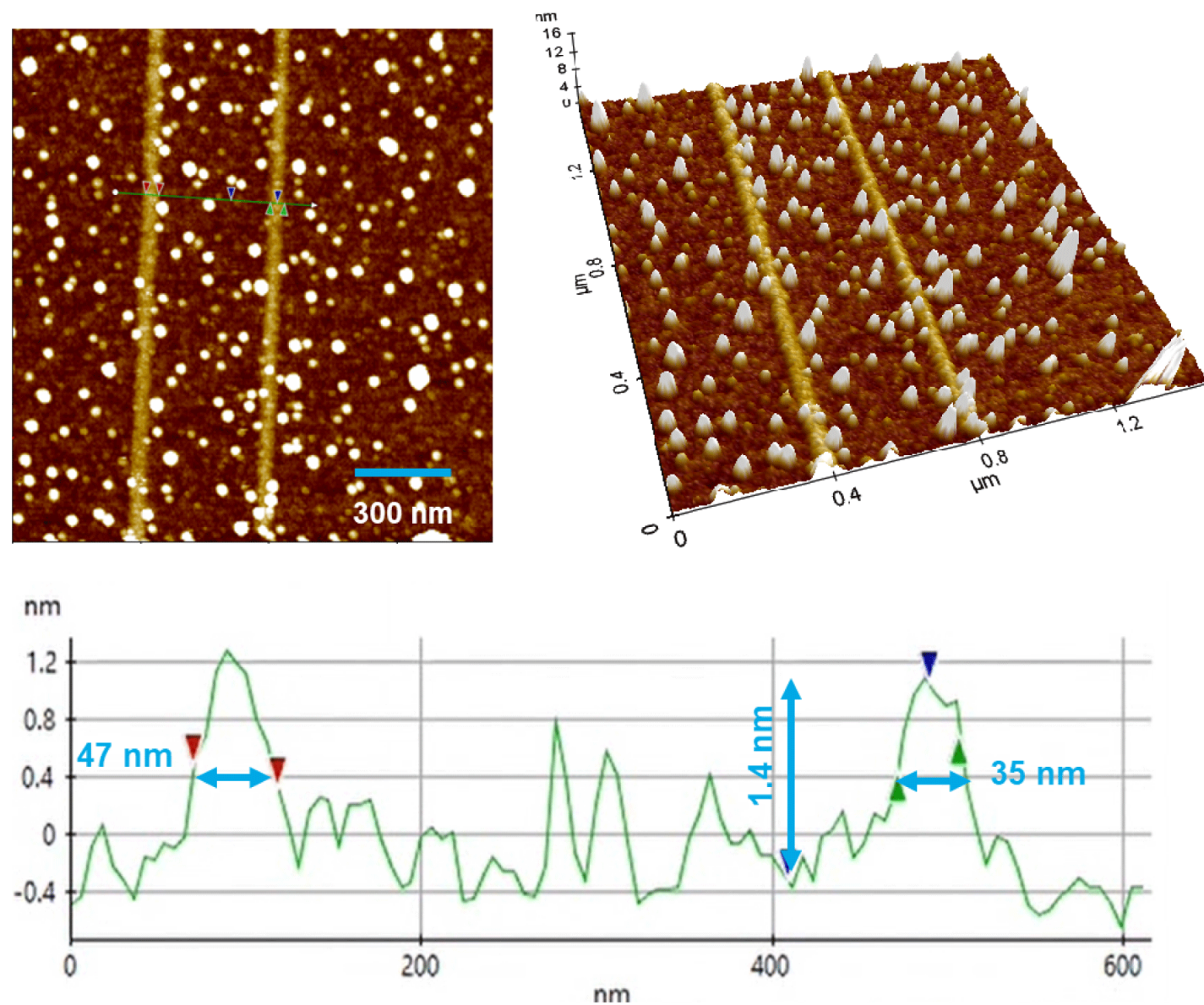


Figure 2. Nanolithography process. (Top Left) Post-scan image. (Top Right) 3D View. (Bottom) Line profile plotted of green line seen in Top Left.

Experimental

For this experiment, a Park NX10 AFM was used to perform bias-assisted nanolithography to draw nanopatterns onto a bare silicon substrate. The oxide patterns were formed using Park SmartLitho. Non-contact mode imaging was conducted after the lithography process to confirm the successful fabrication of the oxide patterns on the surface as well as to distinguish the surface difference between the oxide layers and silicon substrate. A conductive AFM cantilever probe (Multi 75G) with a nominal spring constant ($k = 3 \text{ N/m}$) and resonance frequency ($f = 75 \text{ kHz}$) was utilized in these experiments.

The Park SmartLitho consists mainly of five windows and panels that allow the operator to control the complete

lithography process (Figure 1). In the first step, the appropriate alignment of the super-luminescent diode (SLD) and position-sensitive photodetector (PSPD) is verified (Figure 1A). After confirming the correct alignment, the operator selects the control mode; in this case, the setpoint mode was selected. For the anodic oxidation, a bias has to be applied; in this case, the tip was chosen as the desired channel (Figure 1B). In the design area (Figure 1C), the operator can insert the desired figures and shapes using a previous AFM image as a baseline. All embedded figures will appear in the object list (in this case, just one line) (Figure 1D). The operator can change the formation order, and the estimated lithography time for each figure is provided. Finally, for any desired feature, parameters can be changed in the object edit panel (Figure

1E). Parameters such as voltage, load force, stroke speed, extend speed, or lift speed can be modified to obtain different features within the same designed figures.

To start a lithography or manipulation process, a baseline image is needed. In this case, the baseline image already contains one previously-drawn line to compare with the line about to be drawn (Figure 1C). The image is $1.5 \mu\text{m}$ by $1.5 \mu\text{m}$. The sample features small nanoparticles on its surface according to the image taken using non-contact AFM mode.

The lithography process is planned by drawing a shape on the surface utilizing the software. The AFM operating software, Park SmartScan™, provides the operator with offset and easy positioning features. The DC bias lithography process is done

in contact mode, and in this case, a bias of negative 5.0 Volts is applied between the tip and sample. For this experiment, a line was drawn at $0.2 \mu\text{m/s}$ with a 200 nN load force. The drawn line is approximately 1.8 microns in length (Figure 2, Top Left). The process takes a couple of seconds to complete. As the cantilever is compressed to the loading force of 200 nN, the PSPD signal moves up, which visually verifies the applied pressure.

Results and Discussion

Following the lithography process and using Park SmartScan™, the system is switched back to non-contact mode. An AFM cantilever probe is mounted on a piezoelectric bimorph shaker, attached to the AFM head Z piezoelectric scanner. The shaker vibrates the AFM cantilever probe at its resonant frequency, which is automatically selected along with the vibration amplitude. As the probe nears the sample surface, the vibration amplitude decreases. Likewise, as the probe moves away from the surface, the amplitude increases. The Z piezo scanner moves up and down and adjusts its height to maintain a constant vibration amplitude. The height adjustment of the scanner thus reflects the height change on the sample surface. The AFM raster scans and detects the height change point-by-point in the XY-direction to map out the three-dimensional surface topography. The tip approaches the surface, and the image is retaken promptly with the same parameters as the baseline AFM image. The newly drawn line is clearly visible and parallel to the previously drawn line

(Figure 2, Top Left). Notice the image position remains the same, showing the control of the XY-scanner, separate from the Z-scanner, even at smaller scan sizes. In this example, the lithography process is done in contact mode, and therefore, imaging in non-contact mode is an option. However, after the manipulation, it is important to take the image using non-contact mode to avoid disturbing the particles present on the sample.

After verifying the success of lithography process, the final image is taken and exported to the analysis software called Park XEI™ [4]. In this case, we can see that the previously-drawn line is around 35 nm in width, and the newly-drawn one is 47 nm (Figure 2, Bottom). Both lines are drawn using the same lithography parameters. Nevertheless, the line on the right side, drawn first, is observed to be narrower than the oxide line on the left. This might be due to performing the lithography in contact mode. In contact mode, the tip is rubbed against the sample surface as the lines are drawn.

The rubbing can cause the end of the tip to wear out and blunt. The blunted tip can fabricate wider oxide lines than the ones drawn with a sharper tip [1,5].

We can see that the resulting line-height is approximately 1.4 nm for both lines when adding another cursor. Park XEI software is capable of showing a three-dimensional rendering of the image taken (Figure 2, Top Right). With the 3D representation,

we notice that the lines drawn during this oxide growth process have a lower height than the nanoparticles on the surface.

Conclusion

This application note discusses how to use Park SmartLitho™ software to easily design and customize nanoscale oxide patterns using Park NX10 AFM. With only a few seconds of runtime, this simple test case demonstrates a bias-assisted nanolithography process, which successfully generates oxide patterns as narrow as 35 nm in width. Although the process itself employs contact mode, true non-contact mode before and after the operation validates that the new oxide line is indeed parallel to the line in the baseline image. This test case also demonstrates the scanning and imaging precision of Park's XY-scanner. Overall, this study shows that bias mode in Park SmartLitho software is excellent tool for generating well-defined nanoscale patterns and features.

References

1. E. Pinilla-Cienfuegos, et al. Local Oxidation Nanolithography on Metallic Transition Metal Dichalcogenides Surfaces. *Applied Science*, (2016): 250.
2. JP. Pineda, et al., Nanoscale material patterning using atomic force microscopy nanolithography. *NanoScientific*, Vol 18, (2020): 21-23.
3. Park Systems. (2020). Park SmartScan™. California, USA. <https://parksystems.com/products/operating-software/park-smartscan>
4. Park Systems. (2020). XEI Data Processing and Analysis. California, USA. <https://parksystems.com/manuals-software>
5. J. Voves. Nanoelectronics and nanolithography. *Nanocon 20*, (2009): 22-30.

Park SmartLitho™

The easiest operating system available for nanolithography and nanomanipulation

Park SmartLitho, enabled by SmartScan is an AFM based platform that performs nanolithography and nanomanipulation on materials, electrical and electronics devices, nanotechnology and other areas of research.

The next generation of nanolithography and nanomanipulation software combining powerful tools with an easy user interface

ATOMIC FORCE MICROSCOPE

For more information send a message to inquiry@parksystems.com or visit www.parksystems.com

HIGH RESOLUTION IMAGING OF SINGLE PTFE MOLECULES ON TEFLON SURFACE

Vladimir Korolkov

Park Systems UK Ltd, MediCity, Nottingham, UK.

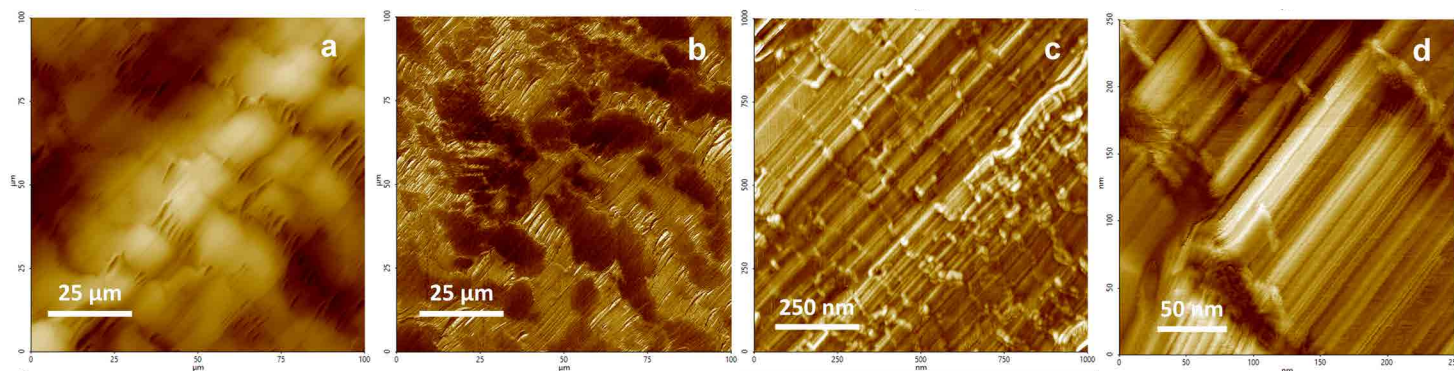


Figure 1. Large-scale height and phase tapping mode images of a Teflon surface. a – height image, 512 x 512 px, scan rate 0.5 Hz. b – phase image acquired simultaneously with image A. c – phase image, 512 x 512 px, scan rate 4 Hz. d – high resolution phase image showing both crystalline and amorphous regions, 512 x 512 px, scan rate 4 Hz. Captured by Park NX20 Large Sample AFM.

Structural studies of polymers are vital, since the application of polymer materials range from micellar drug carriers to bulletproof vests. Their exquisite molecular architecture provides polymers with a variety of unique properties. The ability to image this molecular structure in real-space is, therefore, critical. The only technique that can perform such imaging is Atomic Force Microscopy (AFM).

AFM was developed more than three decades¹. However, it took a long time to utilise AFM to obtain high resolution images of polymers. We can certainly mention the development of torsional tapping to observe single polyethylene molecules by Hobbs and Mullin^{2,3}, bimodal tapping by Proksch⁴ and higher eigenmode imaging by Korolkov⁵. The latter technique, unlike others, does not require any special cantilevers or custom-modified AFM components. In this work, we have implemented this technique on a commercial AFM – Park Systems NX20 – to achieve molecular resolution on a real-world sample of Teflon.

Polytetrafluoroethylene (PTFE), commonly known as Teflon, is a fluorocarbon solid that has one of the lowest coefficients

of friction. Therefore, it is widely used as a material with low adhesion or as an inert coating. Despite its chemical simplicity, PTFE exists in four different crystalline phases that have been studied with electron diffraction techniques^{6,7}. Interestingly, no high resolution AFM data of Teflon have been published to date.

Teflon is known to be a semi-crystalline polymer⁷. Figure 1 shows a set of large scale images of a Teflon surface. A 100 μm x 100 μm image (Fig. 1 a and b) already shows two distinctive areas: large 20 μm domains and rope-like areas connecting them. A closer look at domain areas reveals their highly directional nature. A high resolution phase image (Fig. 1d) shows predominantly crystalline regions separated by smaller amorphous regions on the surface of the polymer. These crystalline domains exhibit flat terraces as observed in Figure 1c and d.

On the following height and phase images (Figure 2), we examine these flat terraces a bit closer. A 100 nm x 100 nm height image (Fig. 2a) shows ~5Å steps with sharp edges. Corresponding phase images (Fig. 2b and c) reveal true molecular nature of these flat steps – we

can clearly resolve single molecules with a period of 5.6Å. A cross-section (Fig. 2d) gives a clear periodic structure of the terrace. From this cross-section, we can also measure the width of a single line at full width at half maximum being 3.5Å. This determines the maximum resolution achieved on this sample. When comparing the observed period of 5.6Å to the reported diffraction data of PTFE unit cell $a = 5.66\text{Å}$ ⁷, we can note a remarkable agreement.

Conclusion

To conclude, we have demonstrated a straightforward practical approach for high-resolution imaging using higher eigenmodes of a standard cantilever in tapping mode on a commercial large-scale NX20 Park Systems AFM achieving molecular resolution of a Teflon sample. AFM, a surface sensitive technique which is always confined to the utmost/outermost surface layer, is able to accurately reproduce results obtained from volume average techniques. Thus, proving that AFM is an important tool in the investigation of the molecular structure of polymers. In fact, AFM is able to provide more structural information by shining a light onto the amorphous

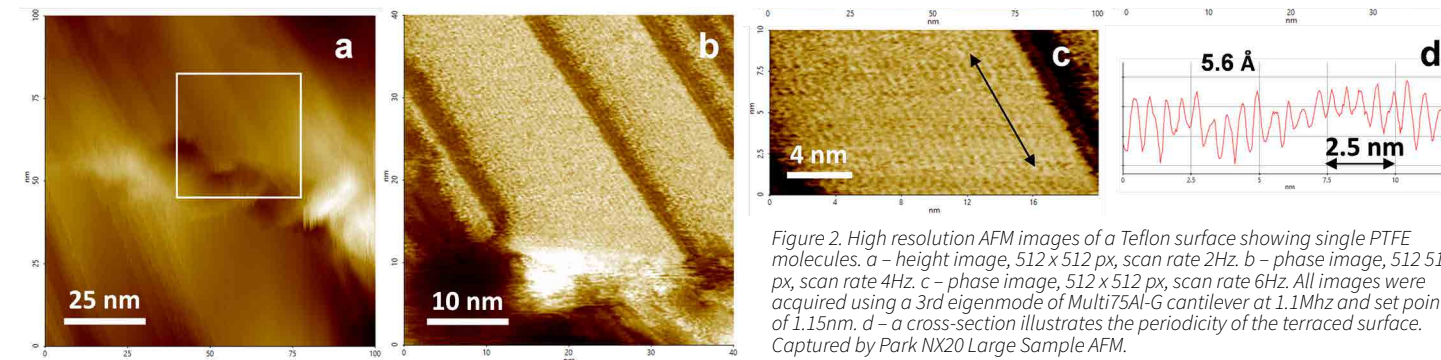


Figure 2. High resolution AFM images of a Teflon surface showing single PTFE molecules. a – height image, 512 x 512 px, scan rate 2Hz. b – phase image, 512 x 512 px, scan rate 4Hz. c – phase image, 512 x 512 px, scan rate 6Hz. All images were acquired using a 3rd eigenmode of Multi75Al-G cantilever at 1.1MHz and set point of 1.15nm. d – a cross-section illustrates the periodicity of the terraced surface. Captured by Park NX20 Large Sample AFM.

regions of Teflon – something that diffraction techniques cannot easily achieve. For instance, a phase image (Fig. 2b) shows that PTFE molecules extend from well-ordered crystalline regions to the amorphous region of the polymer. The highly localized and high resolution nature of AFM places it in a unique position to investigate the structure of polymers in real space.

Read more and join the “Polymer World via AFM” Webinar Series: www.parksystems.com/polymerworld

References

1. Binnig, G., Quate, C. F. & Gerber, C. Atomic Force Microscope. Phys. Rev. Lett. 56, 930–933 (1986).

- Mullin, N. & Hobbs, J. Direct Imaging of Polyethylene Films at Single-Chain Resolution with Torsional Tapping Atomic Force Microscopy. Physical Review Letters vol. 107 (2011).
- Mullin, N. et al. “Torsional tapping” atomic force microscopy using T-shaped cantilevers. Appl. Phys. Lett. 94, 173109 (2009).
- Kocun, M., Labuda, A., Meinhold, W., Revenko, I. & Proksch, R. Fast, High Resolution, and Wide Modulus Range Nanomechanical Mapping with Bimodal Tapping Mode. ACS Nano 11, 10097–10105 (2017).
- Korolkov, V. et al. Ultra-high resolution imaging of thin films and single strands of polythiophene using atomic force microscopy. Nat. Commun. 10, 1537 (2019).
- Clark, E. S. The Crystal Structure of Polytetrafluoroethylene, Forms I and IV. J. Macromol. Sci. Part B 45, 201–213 (2006).
- Brown, E. N., Clausen, B. & Brown, D. W.

In situ measurement of crystalline lattice strains in phase IV polytetrafluoroethylene. J. Neutron Res. 15, 139–146 (2007).

Contact:
Vladimir Korolkov
Park Systems UK Ltd, MediCity, Nottingham, UK.
pse@parksystems.com
www.parksystems.com

Park
SYSTEMS

2021 NanoScientific Forum Europe

Scanning Probe Microscopy (SPM)

15 - 17 September, 2021 | University of Freiburg, Germany

REGISTER for NSFE 2021 TODAY

Conference Topics

- Nanophotonics, nanoelectronics and photovoltaic applications
- Semiconductive materials: organic, inorganic and hybrid
- Nanomaterials and biotechnology
- Electrochemistry for material science
- Overcoming barriers in AFM
- Special Session: Nanotribology via Scanning Probe Microscopy and its applications

SPM Methods:

- Nanomechanical and electrical characterization
- Characterization of soft materials in liquid environment
- Advanced imaging
- High resolution imaging

www.nanoscientificforum.com

SPONSORED BY

Park Systems AFM - Highest Resolution, Accuracy and Ease of Use Brilliantly Combined

Park Systems creates the world's most accurate line of nanoscale microscopy and metrology tools for research and industrial applications. Our innovation features, such as True-Non Contact™ mode and cutting-edge automation, set our products apart from the competition and make Park Systems AFMs the easiest to use and most advanced AFMs available.

General AFMs

Park Systems provides a range of popular AFMs for general research and industrial applications. Designed to be extremely versatile while still providing the accuracy and functionality necessary to do high quality work, our line of general AFMs offer researchers and engineers alike the ability to get extremely accurate results quickly and easily.

Applications:

- Biological Science
- Materials Science
- Failure Analysis
- Semiconductor Analysis
- Hard Disk Media Analysis

Small sample AFM



Park XE7

True research-grade AFM for the practical budget



Park NX10

The world's most accurate easy-to-use research AFM



Park NX-Hivac

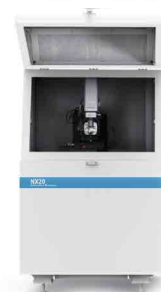
The most advanced high vacuum AFM for failure analysis and sensitive materials research

Large sample AFM



Park XE15

Capable, adaptable, and affordable-the best value large sample AFM



Park NX20

Power, versatility, ease of use, brilliantly combined for large sample AFM



Park NX20 300mm

The leading automated nanometrology tool for 300 mm wafer measurement and analysis

Bio and Chemical

Biological research is one of the fastest growing fields of the 20th century. Park AFMs have played critical roles in this sector, giving researchers the tools they need to develop novel insights into the vast and complicated processes and structures of biology.



Park NX10 SICM

Cutting-edge nanoscale imaging in aqueous environments



Park NX12-Bio

Three compelling nanoscale microscopies in one innovative platform



Park NX12

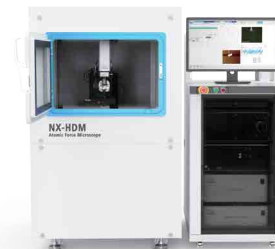
The most versatile AFM for analytical and electrochemistry

Industrial AFMs

Park Systems is dedicated not just to advancing research, but industry as well. That's why our designers have worked to build a line of the most effective AFMs for FA engineers and industrial applications. Allowing users to take highly accurate measurements and complete their work more quickly, these tools can improve efficiency in the workplace and reduce errors, leading to a more profitable, more consistent development and production process.

Applications:

- Failure Analysis
- Semiconductor Analysis
- Hard Disk Media Analysis



Park NX-HDM

The most innovative AFM for automated defect review and surface roughness measurement



Park NX-PTR

Fully automated AFM for accurate inline metrology of hard disk head sliders



Park NX-Wafer

Low noise, high throughput atomic force profiler with automatic defect review



Park NX-3DM

Innovation and efficiency for 3D metrology

APPLICATION-SPECIFIC CHARACTERIZATIONS AND ANALYSES OF CARBON-BASED MATERIALS UTILIZING DIFFERENT MICROSCOPIC TECHNOLOGIES

Manoj Aravind Sankar1*, Prasanna Ram2

1University of California Los Angeles, Los Angeles, California 90095, United States of America
2Vel Tech Rangarajan Dr.Sagunthala R&D Institute of Science and Technology, Avadi, Chennai, Tamil Nadu 600062, India
*Corresponding author: manoj1508.aravind@outlook.com

Abstract

Carbon-based materials are being used increasingly in various applications recently. This is primarily attributed to their customizable nature and multiple allotropes. Carbon could be sourced naturally as well as produced by synthetic methods for the further processing steps into customized forms such as sheets, wires, quantum dots, powder, granules, pellets, rods, tubes, composites, etc. From the viewpoint of the system working cycle, behavioral characterizations are essential to substantiate the applicability of a material. Several analytical and characterization techniques are effectively put into use towards qualitative as well as quantitative estimation, measurement, and verification. In this study, powdered activated charcoal (activated carbon), lampblack (carbon black), and powdered graphene (graphene) are subjected to investigations such as x-ray diffraction (XRD), light microscopy (LM), scanning electron microscopy (SEM), infrared (IR) thermal imaging, electrical probing (Ω), and chemical sampling, and the observations are assessed and correlated with pertinent applications.

Keywords: Characterization, Carbon black, Activated carbon, Graphene, Material.

Introduction

Carbon exists abundantly in various forms which could be acquired, synthesized, and tailored towards their interesting physicochemical, thermal, mechanical, electrical, magnetic, and optical properties. The current study attempts to underline the efficacy of various characterization methods and relate them to carbon's appositeness in multifaceted applications [1,2,3,4].

Materials and Methods

Lampblack is synthesized from Panchadeepa oil, a heterogeneous lipid constituted by ghee and plant oils, subjected to incomplete combustion and vapor-deposition upon copper. Activated charcoal (medicinal grade) was procured from HealthVit. Industrial-grade graphite was acquired and exfoliated into graphene. Tetrahydrofuran (THF), Dimethylformamide (DMF), and distilled water (AR/ACS) were sourced from the Organic Chemistry Laboratory, Veltech Research Park. Indian Pharmacopoeia grade paraffinum liquidum was obtained from Tudor Laboratories [5]. XRD scan was conducted on Bruker instrument with copper anode, $K\alpha_1 = 1.5406 \text{ \AA}$, $K\alpha_2 = 1.5444 \text{ \AA}$ along the goniophotometer axis from 100 - 900 for every 0.020, and analyzed on OriginLab.

Eastcolight HK Micro-Science light microscope was used to capture light micrographs of the carbon materials placed on a microscope slide, with 600-1200x magnification. After image optimization, photos were taken using Xiaomi Redmi Note 3 Pro smartphone equipped with 16 MP and phase-detection autofocus. Image post-processing was done using LunaPic.

SEM was performed with Tescan VEGA 3SBH at an accelerating voltage of 15 kV, working distance 15.16-15.62 mm. After adjusting the optimized image, magnification, average view field, and resolution were set to 1kx, 126.5 μm , and 20 μm , respectively.

Carbon samples were refrigerated at 277K, and then thermal imaging was done using Fluke Ti100 IR Camera. The IR images were interpreted on Fluke SmartView IR Analysis Reporting Software [5].

Electrical resistances of the carbons in liquid paraffin were measured using Crenova MS8233D Multimeter [5].

For testing solubility, 5 mg of each solute was mixed in 100 mL of each solvent - water, 90% THF, 90% DMF, and IP liquid

	Crystalline peaks ($^{\circ}2\theta$)	Amorphous peaks ($^{\circ}2\theta$)	Crystallite size (nm)	% Crystallinity
Activated carbon	50	24, 44, 79	34.33	0.06
Carbon black	30	24, 44	15	2.133
Graphene	26.8	44, 79	13.54	85.56

Table I. XRD Peak Analysis

Results and Analyses

XRD of carbon materials corroborates the crystalline nature. From Table I, it is deduced that the % crystallinity in Graphene >>> Carbon black > Activated carbon. The crystallite size of carbons is in accordance with the amorphousness, i.e., Activated carbon > Carbon black > Graphene.

LM resolution limits its depth of analysis, and hence, properties such as particle size distribution, porosity, surface topography cannot be quantified to a large extent. From Figure 1, the morphology is very uniform for Graphene > Activated carbon > Carbon black. Carbon black spreads erratically, forming layers and shadows in imaging. Activated carbon and carbon black have a higher surface area than graphene since, for an equivalent quantity, graphene is less scattered. Powdery form yields a more pronounced airgap in activated charcoal [5].

SEM images in Figure 2 offer more quantifiable and scalable data than LM. Secondary electron detectors demonstrate topographical variations - clustery porous activated carbon and carbon black, and fractal periodic flaky graphene. Graphene and activated carbon have voids, whereas carbon black consists of agglomerates. Backscattered electron detectors construe the elemental composition as image contrast, and the carbonaceousness in Graphene > Activated carbon > Carbon black.

The forward-looking infrared images in Figure 3 indicate a uniform temperature distribution across carbon black and graphene. However, activated carbon coated glass slide exhibits two different temperature distributions, the other distribution being congruent in dimensions but differing by an average temperature of +5K at a distance throughout. This might be due to the amorphous nature of activated carbon and phonon scattering.

The images in Figure 4 correspond to those in Figure 3, with the former being a three-dimensional representation of the latter. The plane into the paper/screen corresponds to the two-dimensional surface of the carbon-coated glass slide, and the normal axis to it represents the temperature variation map. Graphene

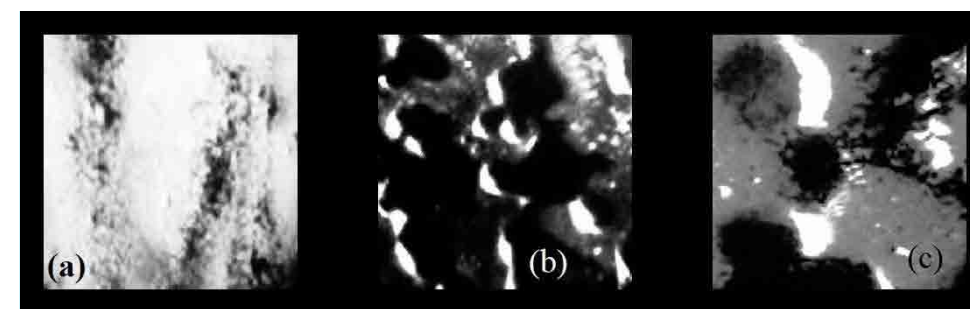


Figure 1. Light micrographs of a) Activated carbon, b) Carbon black, c) Graphene.

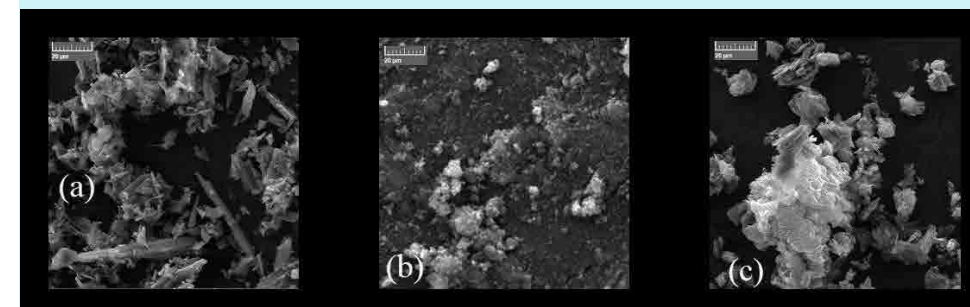


Figure 2. Scanning electron micrographs of a) Activated carbon, b) Carbon black, c) Graphene.

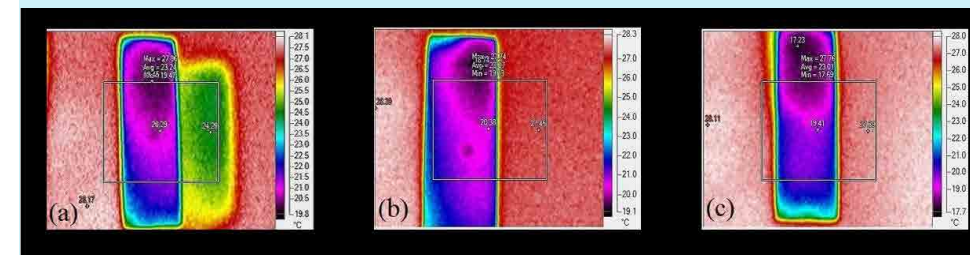


Figure 3. FLIR of microscopic glass slides with a) Activated carbon, b) Carbon black, c) Graphene [5].

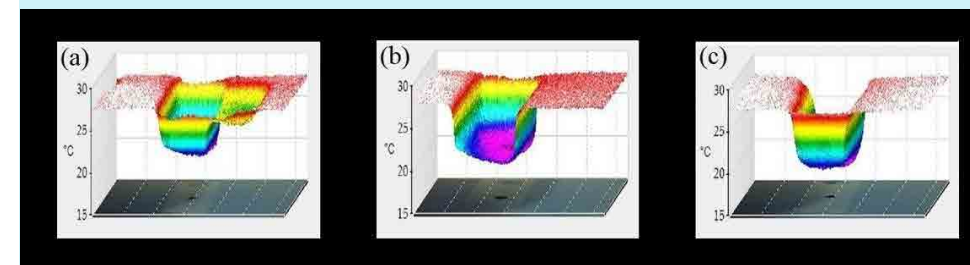


Figure 4. 3DIR graphs of liquid paraffin dispersed with a) Activated carbon, b) Carbon black, c) Graphene [5].

	Water	Liquid paraffin	DMF	THF
Carbon black	Hydrophobic	Suspension	True solution	True solution
Activated carbon	Hydrophobic	Suspension	Colloid	Colloid
Graphene	Hydrophobic	Suspension	True solution	True solution

Table II. Solubilities of carbons in different solvents

Material	Resistance (Ω)
Graphene	$5.6 * 10^3$
Carbon black	$0.35 * 10^6$
Activated carbon	$1.42 * 10^6$

Table III. Ohmic measurements [5]
Resistances in Table III indicate that electrical conductivity of Graphene >> Carbon black > Activated carbon.

and activated carbon exhibit a near-symmetrical heat flux profile. Activated carbon exhibits an enclosed heat variation with the outward heat flux getting flattened, whereas graphene exhibits a similar variation with the heat flux curving outwards in a continuous fashion as it stems from the inward. The heat flux from carbon black is distorted and is asymmetrical.

Solute-solvent molecular interactions vary based on miscibility, homogeneity, and affinity of materials. All carbons repelled water molecules, floating on water in spite of repeated stirring. The three carbons are heterogeneous in liquid paraffin, forming a suspension. Carbon black, after ultrasonication in THF, and graphene exhibit homogeneity with DMF and THF. Activated carbon is averse to THF and DMF. Despite molecular agitation by ultrasonic waves thrice, it exhibited only partial solubility. The observations are briefed in Table II.

Discussion

Material crystallinity, the fundamental of solid-state physics [6], is perceptible from XRD results yielded in Table I. Paramount insights into the morphology, surface topography, stacking, and carbon composition were obtained from the micrographs in Figures 1 and 2, which could be applied in interfacial surface tension in antenna coating [7], platelet formation in layered-printing [8], and conductive filling in voids of ultracapacitor electrode [9]. From Figures 3 and 4, the thermal flux and superficial heat distribution of carbons after cooling were understood, and these would be crucial in passive cooling [10], adsorptive chillers [11], and nanoscale Joule heating [12]. Tangible findings on solute-solvent interactions in Table II furnish helpful observables from the perspectives of industrial pigments, paints, and dyes, and tailoring PEM fuel cell catalyst support towards overcoming platinum catalyst poisoning by hydrophobicity [13]. Electrical resistance measurements would prove nifty in graphene antennas [14] and conductive carbon blacks [15].

Conclusion and Future Scope

In the present work, observations from XRD, LM, SEM, IR imaging, solubility, and Ω were scrutinized and related to carbon applications. The outcomes and impact could be furthered by conducting other

analyses such as TEM, AFM, EDX, Raman spectroscopy, ICP-OES, NMR, TGA, BJH-BET, and molecular dynamics for cumulative supplementation.

Acknowledgment

The authors are grateful to Dr. N.G. Renganathan for his valuable guidance. The authors acknowledge Dr. Gowthaman Swaminathan, Dr. Radhakrishnan Narayanaswamy, Dr. Rameshkumar Chidambaram – former in-charge professors of laboratories, Veltech Research Park (Former Director R&D), and Dr. P. Periasamy and Mr. N. Karunanithi - CSIR CECRI ICP Section Karaikudi for extending their instrumentation and services.

Disclosures

Figures 3 and 4, and Table III are adapted with permission from Ram, P., Sankar, M. A., & Renganathan, N. G. (2019). Studies on Carbon Materials-Based Antenna for Space Applications. In Innovative Design, Analysis, and Development Practices in Aerospace and Automotive Engineering (I-DAD 2018) (pp. 311-329). Springer, Singapore. Copyright 2019 Springer Nature (License #4956790778490).

References

- <https://doi.org/10.1023/B:JMASC.0000021439.18202.ea>
- <https://www.elsevier.com/books/handbook-of-carbon-graphite-diamonds-and-fullerenes/pierson/978-0-8155-1339-1>
- <https://doi.org/10.1002/sml.201102635>
- <https://doi.org/10.1002/adma.201290269>
- https://doi.org/10.1007/978-981-13-2718-6_29
- <https://doi.org/10.1017/CBO9781139167871>
- <https://doi.org/10.1109/TMTT.2011.2164093>
- <https://doi.org/10.1038/srep17707>
- <https://doi.org/10.1016/j.carbon.2018.03.001>
- <https://doi.org/10.1016/j.applthermaleng.2016.03.161>
- <https://doi.org/10.1016/j.apenergy.2013.11.073>
- <https://doi.org/10.1038/nnano.2011.39>
- <https://doi.org/10.3390/nano7020031>
- <https://arxiv.org/abs/1704.00371v2>
- <https://doi.org/10.1016/j.jpowsour.2017.02.056>

Authors' Biography



Manoj Aravind Sankar is currently pursuing MS in Materials Science and Engineering majors at UCLA. He completed his BTech in Electronics and Communication Engineering at Vel Tech University, Chennai, in 2018. His research interests are carbon, materials for energy storage, and biomimicry.



Prasanna Ram currently works as Assistant Professor at Vel Tech University, Chennai. He finished his undergraduate in Adhiparasakthi Engineering College, Melmaruvathur. He completed his postgraduation at SSN College of Engineering, Chennai. He has vast experience in the design of material-based antennas and antenna design for space applications. He is working on a variety of funded projects related to antennas and graphene-printed electronics.

APPLICATION NOTE

IMPROVED ELECTRICAL CHARACTERIZATION OF ADVANCED MATERIALS IN HIGH VACUUM



John Paul Pineda, Charles Kim, and Byong Kim
Park Systems Inc., Santa Clara, CA USA

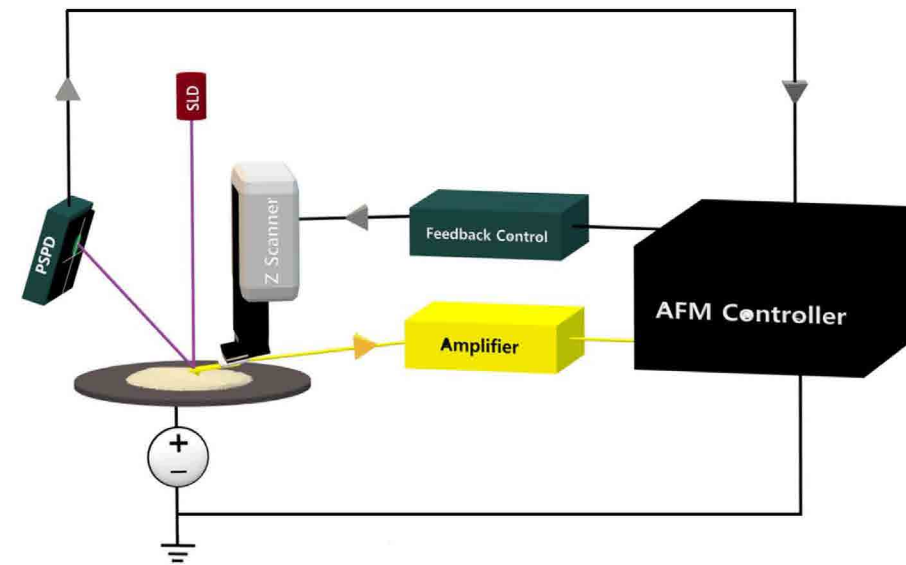


Figure 1. Schematic Illustration of C-AFM and SSRM AFM

Introduction

Sophisticated, high-performing technology often requires electrical components with advanced material properties [1]. For example, TiO₂ thin film, a versatile compound, is widely used as a charge selective transport layer in solar cells and as a high capacity anode for Li-Ion batteries. For battery applications, this material exhibits superior cycling stability and Coulombic efficiency compared to other transition oxides [2]. Another functional material used in advanced technology components is SiC, which is applied in power devices to improve dielectric breakdown field strength, bandgap, and thermal conductivity [3]. For the battery and semiconductor industries to conduct nanoscale electrical measurements during manufacturing, an innovative and precise nanoscale characterization technique for electrical analysis is required.

Conductive Atomic Force Microscopy (C-AFM) and Scanning Spreading Resistance Microscopy (SSRM) are effective techniques for studying electrical properties of advanced materials. These techniques measure electrical

properties by monitoring the current flowing between the conductive tip and the sample during topography measurements. Sensitivity in these techniques can be further improved by controlling the measurement environment. A previous study shows that using C-AFM in a vacuum environment eliminates the layer of contaminants (water and hydrocarbons) that form on the tip, and prevents oxidation during scanning, allowing for a longer tip lifetime and better sensitivity [4, 5]. In this technical note, a study of two different samples with the Park NX-Hivac atomic force microscope demonstrates the advantage of a high vacuum environment for C-AFM and SSRM measurements. The results show improved sensitivity and resolution in the measurements under high vacuum conditions when compared to ambient air.

Experimental

Two samples are selected and investigated using a Park NX-Hivac system. The first sample is a Silicon Carbide (SiC) MOSFET and the second sample is a TiO₂ thin film deposited on a Au/Ti/SiO₂ substrate, hereafter referred to as Sample 1 and Sample 2, respectively. Images for Sample

1 are acquired in SSRM Mode using a scan rate of 0.5 Hz and a scan size of 1.5 μm x 1.5 μm . Images for Sample 2 are acquired in C-AFM Mode with a scan rate of 1.0 Hz and a scan size of 1.5 μm x 1.5 μm . In SSRM imaging, a full diamond tip CAMS FDP (nominal spring constant $k = 27$ N/m) is used, while a CDT-Contr (nominal spring constant $k = 0.5$ N/m) is used in C-AFM. A silver paste is applied on top of the sample, as well as on the metal sample holder under the sample to ensure electrical connection from the bias line. The samples are measured under ambient air and vacuum (in the low 10⁻⁵ Torr range) conditions to understand the influence of the environment on C-AFM and SSRM measurements.

C-AFM and SSRM operate in the Contact mode regime, and their imaging principles are relatively similar. When DC bias is applied, the current flow between the conductive tip and sample is monitored, and the electrical properties are measured. The conductive tip acts as an electrode. Generally, the current has a very low magnitude; therefore, a current amplifier is needed to amplify the current signal. The current amplifier both increases and monitors the current, which is then processed into an image. In this experiment, the applied DC bias is +2.5 V for Sample 1 and +4 V for Sample 2. The main differences between the two techniques are their applications, and the type of current amplifiers needed. C-AFM is commonly used for current variations mapping, while SSRM measures the local resistance and conductance of a surface. The SSRM mode of Park Systems uses a logarithmic current amplifier to measure a wide range of resistance distribution in a small area. In contrast, C-AFM mode uses a linear current amplifier.

Figure 1 shows a schematic view of a C-AFM and SSRM set-up on the Park NX-Hivac system. The AFM cantilever tip, coated with a conductive material,

connects to a current amplifier and can thus measure a wide range of current signal. The current amplifier measures the electric current flow at the tip-sample contact point. As in other AFM modes, the super luminescent diode (SLD) light beam and position sensitive photodiode (PSPD) serve as feedback (Feedback Control) to detect topographic features. The AFM controller then measures and processes these changes to obtain the topography and electrical current C-AFM or SSRM image.

Results and Discussion

Figure 2 presents topography and resistance images of Sample 1 obtained in ambient air and high vacuum using SSRM mode. The topography images in Figures 2a and 2b show a polished surface with a height difference of 109 nm on the cross-section. However, they do not contain significant information related to the device pattern. The measurement positions in both images are the same in ambient air and in high vacuum, as can be seen in their matching topography line profiles in Figure 2c. Therefore, environmental comparison is possible. Figures 2d and 2e are the resistance images taken simultaneously with the topography images in Figures 2a and 2b, respectively. By Figures 2d and 2e, the resistance image taken in high vacuum shows more features and details than the one taken in air. In fact, line profiles of the resistance images, as shown in Figure 2f, show a significant difference in the resistance distribution in air and vacuum. Since there is no oxidation or water layer in the vacuum, the SSRM shows a higher sensitivity in a vacuum than in air due to the improved electrical contact between the tip and sample. Characterizing electrical properties with this level of detail is essential for understanding the functionality of a MOSFET device.

Figure 3 presents the current images of Sample 2 obtained in ambient air and high vacuum using C-AFM mode. Small grain-structures with distinct contrast are visible in the current image obtained in high vacuum, while the current image in air shows less detail. The maximum current measured in high vacuum is 827 nA, while it is 59 nA in air. The line profiles of the current images, as shown in Figure 3c, confirm that a consistently larger current is measured in high vacuum than in air. This improved electrical sensitivity in high vacuum is

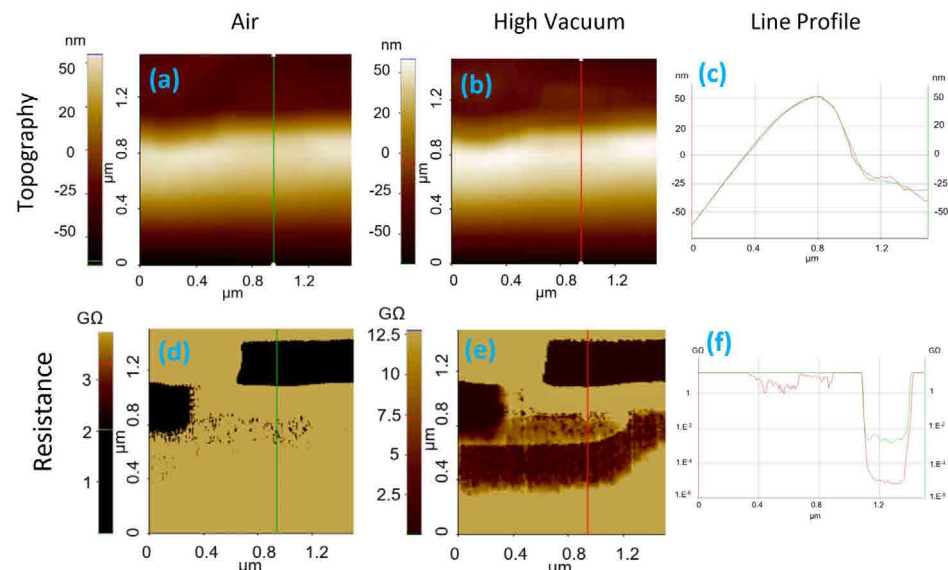


Figure 2. Topography and resistance images measured on a SiC MOSFET sample in ambient air and high vacuum using SSRM mode. (a) Topography in air (b) and vacuum (c) and the corresponding line profiles.

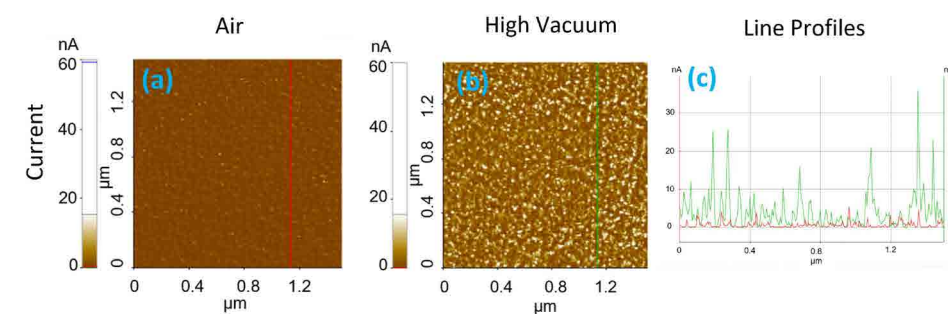


Figure 3. Current images measured in TiO₂/Au/Ti/SiO₂ sample in ambient air and high vacuum using C-AFM mode. (a) Current image in air (b) and vacuum (c) and the corresponding line profiles.

likely due to the removal of water and contaminants that are typically present on the sample surface in air.

Conclusion

This application note examines the current image quality of the SSRM and C-AFM modes of the Park NX-Hivac atomic force microscopy system. Two samples, a SiC MOSFET and a TiO₂/Au/Ti/SiO₂, are tested under ambient air and high vacuum conditions to study the sensitivity of electrical measurements using both modes. The results show that in high-vacuum environments, the sensitivity of the electrical characterization improves. In a high vacuum, the residues are relatively negligible, which increases the electrical contact at the tip-sample surface. Therefore, the current can pass more freely and expose the current contrast of smaller features with a higher definition. In conclusion, operating the Park NX-Hivac system in high vacuum offers detailed insights for various nanotechnology applications and allows for a better

understanding and control of the electrical behavior of advanced materials and devices at the nanoscale.

References

1. J. Puetz, et al., Characterization of Electrical Properties. DOI: 10.1007/978-3-319-19454-7_52-1
2. M. Madian, et al., Current Advances in TiO₂-Based Nanostructure Electrodes for High Performance Lithium Ion Batteries.
3. ROHM Semiconductor, SiC Power Devices and Modules Application Note. Issue of August 2014 14103EBY01.
4. L. Aguilera, et al., Influence of vacuum environment on conductive atomic force microscopy measurements of advanced metal-oxide-semiconductor gate dielectrics. DOI: 10.1116/1.2958246.
5. J. Ludwig, et al., Advantages of High Vacuum for Electrical Scanning Microscopy. https://parksystems.com/images/media/appnote/App_Note_36_Advantages-of-High-Vacuum-for-Electrical-Scanning-Probe-Microscopy_correctionsIH_JS_1.pdf



QUANTIFYING EPITAXIAL GROWTH USING A PURELY TOPOGRAPHICAL SIGNAL

Kai Trepka, UCSF School of Medicine, 533 Parnassus Ave, San Francisco, CA 94143

Abstract—Thin films are ubiquitous, with uses ranging from optoelectronics to antibacterial coatings. Unfortunately, precisely quantifying how the choice of substrate influences epitaxial growth remains an unsolved problem. Here, a novel thin film of holmium oxide with record-high paramagnetic saturation was grown on a variety of substrates. Conventional attempts to extract epitaxial information to characterize the growth mechanism were ineffective, due to the unique size regime of the product. Instead, a signal-processing inspired Fourier method was used to elucidate information on epitaxial ordering from purely topographical data, avoiding the pitfalls of atomic-level diffraction. Further, we define and utilize an inner product-based metric termed a q-score that can quantify the relative degree of ordering of epitaxial crystallites. The q-score provides a direct measure of epitaxy, enabling more quantitative future studies of thin film growth.

INTRODUCTION

Magnetic resonance force microscopy (MRFM) is an emerging technology that offers the promise of single nucleon detection in individual biological samples or nanodevices [1]. Such a device functions like a nanoscale magnetic resonance imaging (MRI) machine, applying a radiofrequency (RF) current and measuring response with a magnetic cantilever, all against the background of a strong uniform magnetic field [2,3]. Effective MRFM demands a large signal to noise ratio (SNR). From [3], this is:

$$SNR = \frac{N\mu_N^2}{2\Delta f k_B T} \left[\left(\frac{\partial B}{\partial x} \right)^2 \left(\frac{w_c Q}{k_c} \right) \right] \quad (1)$$

Since the SNR is quadratically dependent on the magnetic field gradient $\partial B/\partial x$, developing strong, new magnetic materials is important for optimizing

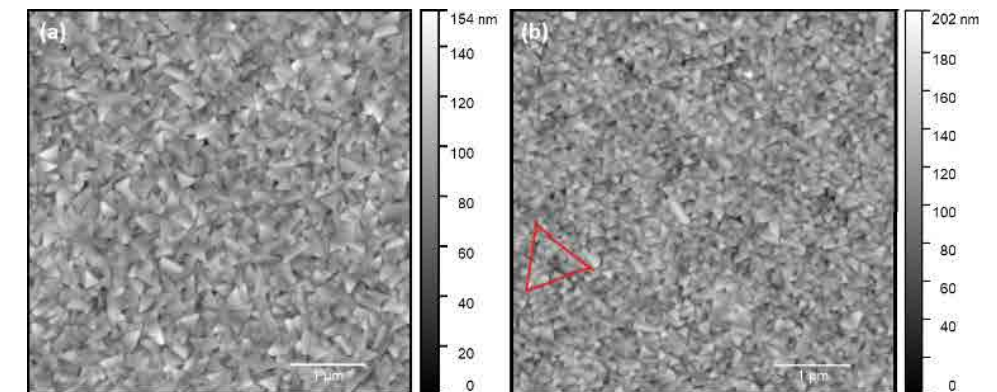


Fig. 1. Atomic force micrographs of holmium oxide thin film growth on Sapphire A (a) and Sapphire C (b) substrates. Upon visual inspection, the triangular crystallites appear to be randomly oriented with respect to one another in (a), but roughly aligned with the drawn red triangle in (b).

MRFM. Recently, a new crystal phase of holmium oxide thin film with record-high paramagnetic saturation (above 2 Tesla) was synthesized using a thermal physical vapor deposition technique [4]. Holmium films grown on different substrates (A-plane sapphire, C-plane sapphire, and amorphous quartz) under otherwise identical deposition conditions have different morphological properties, suggesting that the substrate controls film growth. This direction is not a chemical process, as the two sapphire substrates are chemically identical, and growth occurs in a regime well below the vaporization of all the substrates [5,6]. Rather, the different crystal structures and orientations of the substrates visually appear to direct holmium growth in different ways. For example, in Figure 1, we see the holmium oxide film grows into crystalline triangles regardless of surface, but on the Sapphire C substrate (Fig. 1b), they seem to be aligned with one another.

When thin films grow, individual atoms land on the surface and then move around until they lose their kinetic energy and reach a thermodynamic minimum [7]. This can occur in different ways depending on how the landing atoms align with the substrate crystal atoms.

When films grow on a substrate, the substrate can direct their growth to align with its own crystal structure, creating a periodic result [8]. This is termed epitaxial growth.

To determine whether different substrates are directing growth of different crystal phases of holmium oxide, we attempted a variety of standard diffraction techniques, including coarse x-ray diffraction (XRD) and more fine-grained elastic recoil detection (ERDA) and transmission electron microscopy (TEM). Most of these techniques determine bulk crystal structure and elemental composition, ultimately determining that we have a new phase of holmium oxide. However, they operate at the wrong size scale to determine whether the crystallites themselves are oriented. XRD and ERDA are too coarse to detect individual crystal grains reliably [9,10]. Available TEM only operates at a small domain size (~50 nm), while the crystallites in question are on the order of 100 nm. Although TEM has been successful at studying epitaxial growth in the past, it has traditionally been done on much thinner and smaller nanostructures [11] or been focused on defects [12]. In other words, no techniques were successful at revealing the orientation of individual crystal grains

relative to each other, which is key to understanding the influence of using different substrates on holmium oxide growth and designing future experiments.

Fortunately, techniques from signal processing can be used to uncover periodicity that is otherwise not apparent in images. In particular, the 2-dimensional Fourier transform is a promising tool and is defined by the relation in Equation (2). While the most common transforms in signal processing work by converting between time and frequency domains, the 2D transform here operates between two spatial regimes: real, physical space, parametrized by x, y , and inverse k -space, parametrized by u, v . By converting the image from real space into k -space using an orthogonal basis of complex exponentials, patterns emerge that can be used to quantify how ordered the substrate is [13]. In particular, the discrete Fourier transform (DFT, defined by Equation (3)) of an image is readily implemented using an FFT algorithm in MATLAB, as described in [14].

$$F(u, v) = \int_{-\infty}^{\infty} \int_{-\infty}^{\infty} f(x, y) e^{-j2\pi(xu+yv)} dx dy \quad (2)$$

$$F[u, v] = \frac{1}{XY} \sum_{x=0}^{X-1} \sum_{y=0}^{Y-1} f[x, y] e^{-j2\pi(\frac{x}{X}u + \frac{y}{Y}v)} \quad (3)$$

Note that in (3), X is the total number of pixels in the horizontal direction, and likewise for Y in the vertical direction. The discrete transform sums over all available pixels and sets $f[x, y]=0$ outside the observed X by Y region.

Quantifying epitaxy has applications beyond holmium oxide thin films. Thin films are ubiquitous [15], with applications ranging from optoelectronics as in [16] to antibacterial coatings as in [17]. In general, quantifying the influence of substrate on thin film growth, termed epitaxial growth, is a challenging problem [8,18]. Most literature relies on expensive atom-level measurements and can only detect a few layers of atoms (~1 nm) worth of epitaxial growth [11,12,19], while thin films with practical applications are often over 100 nanometers thick [20].

Here, we develop and test a facile classification scheme that quantifies how ordered thin film growth is using only topological data. This approach relies on transforming topographical atomic force microscopy (AFM) data into k -space and

comparing the result to the predicted Fourier transform of perfect thin film epitaxy, as well as measuring maintenance of periodicity over large regions of film.

The following notation will be used throughout the manuscript:

$f[x, y]$ denotes the z -height/brightness at a given spatial coordinate of an AFM image

$F[u, v]$ denotes the transform of $f(x, y)$; this is the FFT in all cases except in section V.

$\langle A, B \rangle$ denotes a Frobenius inner product

A^* denotes the complex conjugate of A

TOPOGRAPHICAL CRYSTALLINITY

It is well known that using different substrates can result in the growth of different types of crystal grains. There are three main cases of thin film growth, reviewed extensively in [8] and [15].

Epitaxial crystalline growth. In the case of epitaxial growth, the crystal grains align perfectly with the substrate's crystal structure, and the edges of crystal grains also align with the substrate and thus align with each other. Topographical data of this type of growth presents as a perfect tessellation of crystal edges. The shape of the grains depends on the shape of the substrate's exposed crystal plane.

Non-epitaxial crystalline growth. In the case of non-substrate directed crystalline growth, nucleation and growth occurs in random directions. Although crystals with hard edges can still form, they will not be aligned with each other. This can be modeled as an assortment of randomly oriented crystals, where the shape of the crystal depends mostly on the thin film material's intrinsic crystalline properties.

Random growth. In the case of non-epitaxial, non-crystalline growth, the thin film grows haphazardly on an unordered substrate, forming unordered structures. This case is largely non-instructive, and has no consistent morphological ordering.

In this experiment, holmium oxide was grown on two different crystal planes of sapphire, A-plane and C-plane, depicted in Fig. 2. The A-plane atomic cross section is a rectangular lattice, while the C-plane cross-section contains a hexagonal lattice. Meanwhile, holmium naturally

grows into a hexagonal lattice [21] that is a close match in terms of lattice strain to C-cut sapphire, so it is expected that the C-plane sapphire will clearly direct its growth, whereas holmium will grow into randomly oriented triangular or hexagonal crystallites on the A-plane sapphire. The amorphous quartz substrate is not crystalline, and thus cannot epitaxially direct growth.

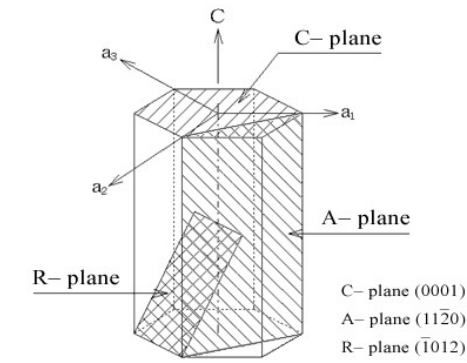


Fig. 2. Different sapphire crystal planes. C-plane sapphire is a hexagonally symmetric lattice, while A-plane sapphire is more rectangular.

Since there should be one main set of periodic components in the first case, and many rotated sets of the same kind of triangle in the second case, the 2-dimensional Fourier transform (FT) offers a way to extract the magnitude of different periodic components and quantify underlying periodicity. The 2D FT is based on the same principles as a one-dimensional Fourier transform, using complex exponential functions of x and y as the basis set.

Since we have discrete images of 512x512 datapoints, we have to use the DFT described in Equation (3) rather than the FT described in Equation (2), with $X=Y=512$. Note that this transform works theoretically because the AFM signal is viewed as a multiplication of the real thin film surface with the bed-of-nails function in Equation (4), which samples out 262,144 discrete datapoints from the true, underlying, continuous thin film surface.

$$\sum_{n=-\infty}^{\infty} \sum_{m=-\infty}^{\infty} \delta(x - nX) \delta(y - mY) \quad (4)$$

Implementing the FFT in MATLAB on a representative set of potential crystal patterns, it is apparent that the FFT of disordered triangles contains the

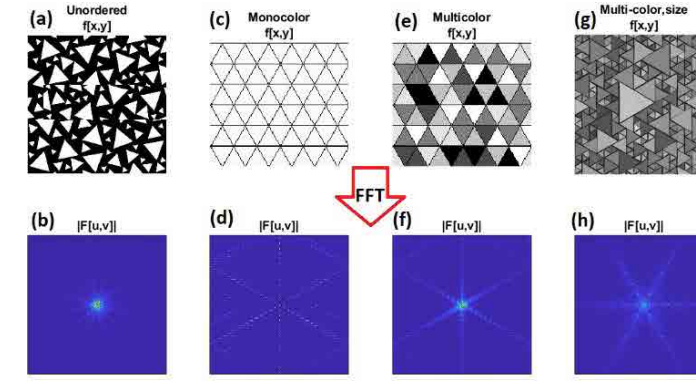


Fig. 3. Theoretical Fourier domain images of ordered (epitaxial) vs disordered (non-epitaxial) triangles. (a), (c), (e), and (g) depict initial images, while (b), (d), (f), and (h) are their respective FFTs. In (a) and (b), the unordered triangles create a mess of overlapping, rotated hexagons. In (c) and (d), a uniform, perfectly ordered tessellation of identical equilateral triangles creates rhomboidal patterns out of discrete dots. In (e)-(h), tessellations of triangles of varying height and size both create hexagonal FT patterns.

superposition of many rotated transforms of individual triangles, ultimately creating a messy (and, ad infinitum, uniform and circularly symmetric) Fourier transform (Fig. 3a-b).

Meanwhile, any set of ordered or tessellated triangles results in six main lines originating from the zero-order center, rotated depending on the initial orientation of the triangles (Fig. 3c-h). The hexagonal symmetry emerging from a central node is most apparent when multicolored triangles are used (Fig. 3e-h). These multicolored images are more realistic representations of crystal grain growth, individual grains grow to varying sizes and thus are different heights in AFM micrographs.

The hexagonal ordering and Fourier pattern appear to be independent of variations in amplitude (color) or size variations in the initial triangle tessellation, suggesting the Fourier transform may be an effective way to classify ordering in crystal growth. Now that it is clear that the different theoretical growth regimes of crystals should be distinguishable using the Fourier transform, the given holmium oxide AFM data can be transformed into k -space and qualitatively compared to the theoretical transforms in Fig. 3.

QUALITATIVELY INVESTIGATING HOLMIUM OXIDE THIN FILM GROWTH

Taking the 2-dimensional FFT of the holmium oxide thin film data yields k -space images that immediately reveal orientation differences between the films grown on A-plane sapphire, C-plane

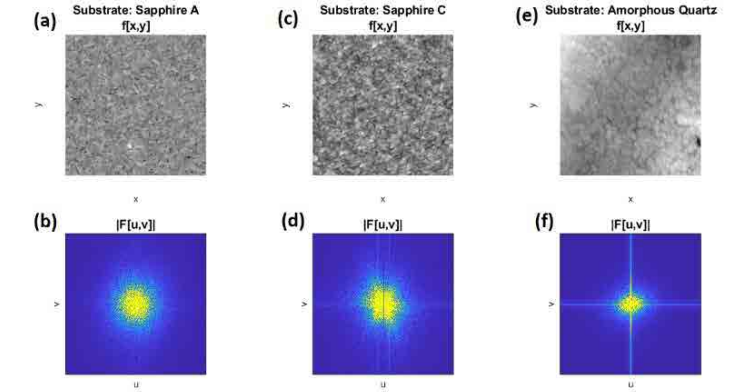


Fig. 4. Holmium oxide thin films grown on three different substrates under identical run conditions and their respective FFTs. The thin film on sapphire A (a), which contains triangular crystallites, has no clear ordering in its FFT (b). However, the thin film on sapphire C (c), which also contains triangular crystallites, has hexagonal ordering in its FFT (d), suggesting crystallite alignment. To contrast, there is no clear ordering in either the AFM image (e) or FFT (f) of the film grown on amorphous quartz, only large zero-order patterns and symmetric spread.

sapphire, and amorphous quartz.

In particular, both films grown on sapphire substrates have considerable spread from the zero-order lines in the Fourier plane (Fig. 4a-d), while the film grown on quartz is clearly disordered optically and has no visible triangles (Fig 4e). The Fourier transform of the film grown on amorphous quartz is focused around the zero-order lines, suggesting more random growth (Fig. 4f).

Note that in the initial AFM image, while it is clear to the eye that the crystallites are triangular on both A sapphire (Fig. 4a) and C sapphire (Fig. 4c), whether these triangles are aligned with each other is an open question. However, the slight qualitative differences in the Fourier domain suggest an answer. While the transform of the holmium oxide film grown on Sapphire A is largely circularly symmetric (Fig. 4b), suggesting some amount of sharp triangular edges but not ordered triangles (similar to the pattern in Fig. 3b), the transform of the holmium oxide film grown on C-plane sapphire has higher brightness along a hexagonal set of contours (Fig. 4d), akin to the theoretical transforms in Fig. 3f and 3h.

While this qualitative comparison of Fourier transforms to the theoretical transforms of tessellations given in Fig. 3 suggests a slight difference in epitaxial ordering between the Sapphire A- and Sapphire C-grown films, it is unclear if there is some fine degree of overall threefold ordering on Sapphire A (which would be possible if, for example, each triangular crystallite constrained the

orientation of the neighboring crystallite; in other words, the holmium could self-direct its own growth.) Thus, quantifying the perceived difference between Fig. 4b and Fig. 4d is important for understanding how ordered the thin films are.

QUANTIFYING EPITAXIAL GROWTH

At present, two tools are widely used to quantify the influence of epitaxy on nanostructure and thin film growth.

Direct measurements using TEM, as in [11] and [12]. This reveals the degree of lattice mismatch at the substrate-film interface and is thus the ideal tool for quantifying epitaxial growth. However, this tool is ineffective when the resulting thin film does not perfectly match up with the sapphire crystal lines (as with the holmium oxide), and when the size regime of interest extends beyond a couple nanometers (in our case, the relevant regime is hundreds of nanometers; see Fig. 1).

Theoretical lattice mismatch [22]. Every material has a known crystal structure, and the difference between lattices (i.e. the size of a holmium hexagon vs a sapphire hexagon) can be computed. Lattice strain s is determined by the crystal spacing of the substrate a_{sub} and intrinsic crystal spacing of the film material a_{epi} in Equation (5). Typically, a lattice strain of below 10% ($s=0.1$) suggests epitaxial thin film growth.

$$s = \frac{a_{sub} - a_{epi}}{a_{sub}} \quad (5)$$

However, this technique is not a true “measurement” of ordering, but rather a convenient percentage that can be reported along with qualitative images of clearly ordered growth (i.e. aligned nanowires). Lattice mismatch does not always determine epitaxial growth and vice versa [23]. For example, the lattice strain between holmium oxide and sapphire C is $s = 0.25 > 0.1$, but it is clear by inspection that choice of substrate influences growth (Fig. 4a,c,e).

As a result, development of a quantification scheme beyond lattice strain that can utilize easy-to-collect topographical data (i.e. from AFM, SEM) is paramount to understanding partial ordering and ordering on large scales.

Once again, tools from signal processing come into play. Rather than qualitatively comparing the FFT of an ordered lattice of triangles with that of AFM images, we can quantitatively compare the two using an inner product.

First, we choose a quantifier, an ideal image and corresponding FFT to model the epitaxy that we would like to measure a given thin film’s similarity to. Note that the choice of quantifier will define our result, so future work must be careful when comparing different results to make sure the same choice of quantifier image was used.

To measure the similarity of a given image with the quantifier, we could simply take a Frobenius inner product (Equation (6)) of the matrix Q representing the FFT of the quantifier and A representing the FFT of the image. If the hexagonal patterns align, this will be larger than if none of the patterns align.

$$\langle A, Q \rangle = \sum_{i,j} A_{ij}^* Q_{ij} \quad (6)$$

However, in order for this computation to work, the FFTs must be pre-processed first. Otherwise, images that are very bright will automatically have a very large inner product, or triangles that are not exactly aligned with those of the quantifier image may have a low inner product despite perfect alignment between triangles in the AFM image.

The quantifier algorithm is as follows:

1. Load the images and take their FFTs.
2. Remove uniform background noise.
3. Remove outliers above an experimentally determined high quantile. In the future, an LPF could be used.
4. Normalize each FFT F by dividing by its Frobenius norm, $\sqrt{\langle F, F \rangle}$, where the inner product is given in (6).

$$q = \langle A', Q' \rangle \quad (7)$$

5. Compute what we here define as the q-score, defined as the inner product of the processed FFTs A', Q' :
6. In addition, compute the error, defined below. Note that low q-scores are correlated with high errors.

$$\epsilon = \sum_{i,j} |A_{ij} - Q_{ij}|^2 \quad (8)$$

There is one further challenge: rotating an image will also rotate the FT of that image. For instance, rotation of the quantifier triangle tessellation image by 10 degrees will also rotate its Fourier transform by 10 degrees. The proof is below:

Working in polar coordinates, set $x=r \cos \theta, y=r \sin \theta, u=\rho \cos \phi, v=\rho \sin \phi$. Plugging this into Eq. 2, we see $F(\rho, \phi)$

$$\begin{aligned} &= \int_0^\infty \int_0^{2\pi} f(r, \theta) e^{-j2\pi(r \cos \theta \rho \cos \phi + r \sin \theta \rho \sin \phi)} r dr d\theta \\ &= \int_0^\infty \int_0^{2\pi} f(r, \theta) e^{-j2\pi r \rho \cos(\theta - \phi)} r dr d\theta \end{aligned}$$

By inspection, a rotation in real space results in the same rotation in k-space, i.e.

$$f(r, \theta + \theta_0) \leftrightarrow F(\rho, \phi + \theta_0) \quad (9)$$

In order to avoid accidental mismatch between potential perfect tessellations of the substrate and quantifier (i.e. the substrate hexagonal pattern could, by chance, be rotated 30 degrees away from the quantifier FFT hexagonal pattern), we will rotate the quantifier by small increments, going through the above algorithm and computing the q-score and error for each rotation. We can perform

this rotation in real space and then take the Fourier transform, as rotating in either basis is equivalent by (9). Then, we select the highest q-score (i.e. the best match) and set that as the true q-score, along with its concurrent error. Note that for a 6-fold symmetric image such as a tessellation of triangles, we only have to rotate through a total of 60 degrees before the original pattern returns, decreasing computational time. In addition, the amount of each rotation can be tuned according to computational demands.

A quick internal calibration of the quantification algorithm is that it should return 1 if $Q=A$; this is indeed the case.

Next, we test this algorithm on our images, depicted in Figure 5. The different quantifiers used are the mono-color image (Fig. 1c), multi-color, -size image (Fig. 1g), and multicolor image (Fig. 1e). Recall that a high q-score is indicative of high matching with the ideal pattern, and subsequent high ordering. While the particular q-scores change depending on the choice of quantifier, the ordering remains the same: sapphire C is the most ordered, followed by sapphire A. Amorphous quartz is the least ordered.

In addition, note that the multicolor, multi-size triangle tessellation quantifier offers the greatest distinguishability. This is expected, given that it is most similar to the AFM pattern that would actually be observed in the case of epitaxial growth: crystallites are all oriented, but can vary in height and lateral size, represented by variations in color and size respectively.

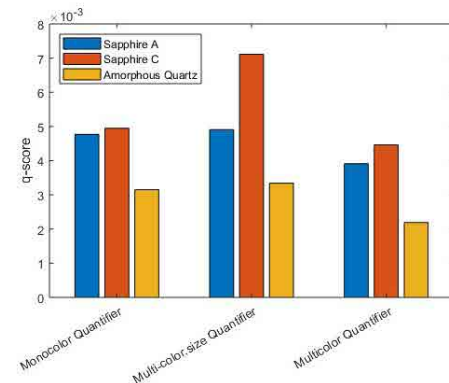


Fig. 7. Computed error of matching for long-range ordering. Sapphire A has much higher error, suggesting less order and less epitaxy.

One additional use of this quantification scheme lies in comparing images to one another. For example, one other

set of data we have is images from each substrate taken 5 mm apart from one another, a measure of long-range ordering. We can then set each image as Q , and define another image taken from the same substrate as A ; in other words, we are taking a version of the inner product between images from different portions of a given substrate. If there is long-range ordering, this q-score should be large; otherwise, it will be small.

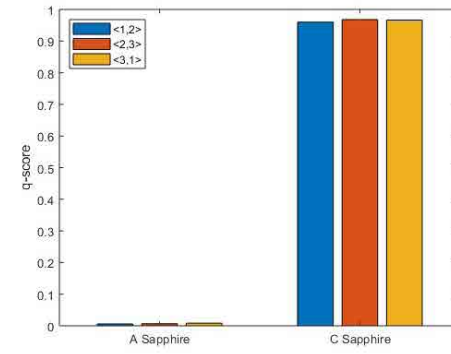


Fig. 6. q-scores of long-range ordering on different substrates. A higher q suggests C has more long-range ordering than A.

Using 3 images from each of sapphire A and sapphire C, each image taken 5 mm from the last along the same line of translation, we compute the q-scores between each permutation of the 3 images. Zero rotation of FFTs is used, as rotation occurring over the course of translation would indicate that the long-range ordering is broken. The resulting q-score for sapphire C is much higher than that of sapphire A (Fig. 6). Thus, the film grown on sapphire C is well-aligned across enormous spatial jumps (5 mm \gg 5 microns, the span of each image). This preservation of ordering over a long range is highly unlikely to occur unless the underlying substrate is directing growth at each point, making this a direct and quantitative measure of epitaxy.

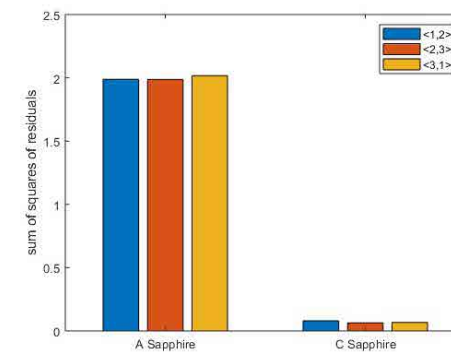


Fig. 7. Computed error of matching for long-range ordering. Sapphire A has much higher error, suggesting less order and less epitaxy.

The error terms, computed using Equation (8), are small for sapphire C, but large for sapphire A (Fig. 7), confirming a poor match in Fourier space between different images from sapphire A and consequent non-epitaxial growth.

One interesting result is that the q-score, when comparing shifted images, approaches 1 for the aligned growths on sapphire C (Fig. 6). This approach utilizes the shifted AFM images as quantifiers. However, the q-score is nearly 1000 times smaller when using an abstracted perfect tessellation as the quantifier (Fig. 5). As a result, the best use of the quantifier algorithm is likely to compute self q-scores, i.e. quantify the difference in Fourier transforms between different regions of a single thin film to detect long-range ordering. This use alleviates one of the biggest problems with the quantifier algorithm: the choice of the ideal quantifier or FFT to compare our signal to. From Figure 5, it is apparent that altering quantifiers can change q-scores by nearly 50%, and that differentiability is sometimes a challenge (i.e. the q-scores of sapphire A and sapphire C are very close for all but the multicolor, multi-size quantifier). Comparing images to their downstream counterparts adds an internal control, which is desirable as the exact pattern of epitaxial growth is unknown due to uncertainties at nanoscale.

One interesting result is that the q-score, when comparing shifted images,

approaches 1 for the aligned growths on sapphire C (Fig. 6). This approach utilizes the shifted AFM images as quantifiers. However, the q-score is nearly 1000 times smaller when using an abstracted perfect tessellation as the quantifier (Fig. 5). As a result, the best use of the quantifier algorithm is likely to compute self q-scores, i.e. quantify the difference in Fourier transforms between different regions of a single thin film to detect long-range ordering. This use alleviates one of the biggest problems with the quantifier algorithm: the choice of the ideal quantifier or FFT to compare our signal to. From Figure 5, it is apparent that altering quantifiers can change q-scores by nearly 50%, and that differentiability is sometimes a challenge (i.e. the q-scores of sapphire A and sapphire C are very close for all but the multicolor, multi-size quantifier). Comparing images to their downstream counterparts adds an internal control, which is desirable as the exact pattern of epitaxial growth is unknown due to uncertainties at nanoscale.

THE DISCRETE COSINE TRANSFORM: ANOTHER WEAPON IN THE ARSENAL?

The success of using the q-score to quantify long-range ordering relies on the transformation of real space to a form of frequency space. Although the Fourier transform was used in the quantifier algorithm, alternative transforms could potentially be used. For example, the discrete cosine transform (DCT) is often

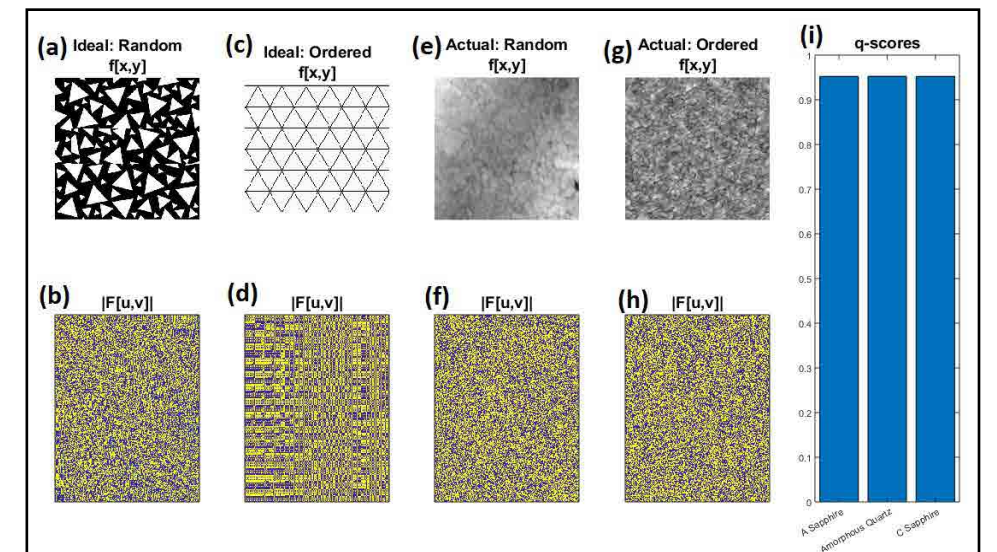


Fig. 8. Applying DCT to epitaxial characterization. (b) depicts the DCT of (a), while (d) depicts the DCT of (c). The ideal ordered triangles have much more “striped” DCT than the randomly oriented triangles. However, this qualitative distinction disappears when comparing thin films grown on sapphire A (e,f) and sapphire C (g,h). (i) depicts the q-scores for the DQA on all substrates; they are virtually identical.

used for lossy image compression, relying on an orthogonal basis of cosine functions (rather than complex exponential functions, as with the FT) [24]. The DCT is defined below, omitting normalizing factors:

$$F(u, v) \propto \sum_{x=0}^{X-1} \sum_{y=0}^{Y-1} f(x, y) \cos \left[\frac{(2x+1)u\pi}{2X} \right] \cos \left[\frac{(2y+1)v\pi}{2Y} \right] \quad (9)$$

We define our DCT quantifier algorithm (DQA) as identical to the previous algorithm, except taking a 2D DCT in all places where a 2D FFT was previously performed. Applying the DQA to a few test cases shows that it is potentially useful, but quantitatively challenging to optimize.

Fig. 8. Applying DCT to epitaxial characterization. (b) depicts the DCT of (a), while (d) depicts the DCT of (c). The ideal ordered triangles have much more “striped” DCT than the randomly oriented triangles. However, this qualitative distinction disappears when comparing thin films grown on sapphire A (e,f) and sapphire C (g,h). (i) depicts the q-scores for the DQA on all substrates; they are virtually identical.

When looking at the discrete cosine transforms of ideal ordered vs unordered triangles (Fig. 8a-d), differences are immediately apparent. The DCT of the unordered triangles in (8a) appears random (8b), while that of the triangular tessellation in (8c) appears to contain more slowly varying outputs and longer regions with the same coefficients, resulting in a striped pattern (8d).

This theoretical qualitatively useful difference disappears when looking at real samples. The transform of the totally random sample on quartz (8e) looks like a pattern of distorted static (8f) not so different than the transform of ordered holmium thin film on sapphire c (8h). Differences invisible to the eye often show up when computing computational similarities when using an inner product; unfortunately, applying the DQA to the three substrates results in virtually identical q-scores (8i), suggesting little quantitative difference when using cosines as the orthogonal basis set for transforming.

Implementation of the discrete wavelet transform (DWT, reviewed in [25]) produces similar results. There are differences between the ideal ordered and random cases, but little immediate quantitative difference with the real films. One final future strategy beyond the scope

of this work is development of a neural network for image recognition of FFTs that can distinguish between epitaxial, partially epitaxial, and non-epitaxial growth [26], which would improve upon the q-score as a metric. Although work has been done to optimize such a network in the case of particular individual thin film materials' growth conditions [27], a larger project could utilize the FFTs of a wide array of datasets known by TEM or other techniques to demonstrate epitaxy, partial epitaxy, or random growth to train the algorithm. This approach would also allow quantification of epitaxy from relatively low-resolution topographical images alone.

CONCLUSION

Because of the broad applications of epitaxially-grown thin films, mechanistically understanding their growth is critical to developing and characterizing new materials. In particular, a set of holmium oxide thin films grown on three different substrates under otherwise identical conditions were found to be exceptionally paramagnetic, but the degree of epitaxy was not measurable via traditional diffraction techniques, inhibiting mechanistic understanding of their growth. However, it was possible to collect extensive topographic data via AFM, and it was obvious that the holmium oxide crystallites appear to exhibit symmetry akin to that of a triangular tessellation.

Here, we developed a qualitative theoretical framework for transformations of ordered vs unordered triangles into k-space, demonstrating 6-fold symmetry for the ordered case and symmetric spreading for unordered triangles. We compared the FFTs of holmium oxide crystallites grown on various substrates to the transforms of these ideal cases, which suggested that growths on sapphire C are epitaxially aligned.

Next, we developed and tested an algorithm for calculating a “q-score”, a modified inner product between FFTs that quantifies the amount of similarity (and thus epitaxial ordering), confirming that sapphire C was indeed more ordered than sapphire A. Since this q-score relies on comparing two images, two approaches can be used: comparing a theoretically ideal transform to any image or comparing different images from the same substrate. The former allows comparison and potential identification of triangular vs other types of symmetry, while the latter allows direct quantification of long-range

epitaxy with a robust internal control. This algorithm was modified to operate using DCTs and DWTs, with some results but little practical quantification success.

Ultimately, the C-sapphire substrate is most effective at epitaxially directing holmium oxide thin film growth, making it a candidate for future experiments. More broadly, utilizing Fourier space enables quantification of epitaxial growth in the absence of crystal data. The q-score as a tool measures and quantifies epitaxial growth, allowing mechanistically guided development of new materials.

REFERENCES

- [1] D. Rugar, R. Budakian, H. J. Mamin, and B. W. Chui. "Single spin detection by magnetic resonance force microscopy." *Nature*, vol. 430, no. 6997, pp. 329, 2004.
- [2] J. Sidles, J. Garbini, K. Bruland, D. Rugar, O. Zuger, S. Hoen, and C. Yannoni. "Magnetic resonance force microscopy." *Reviews of Modern Physics*, vol. 67, no. 1, pp. 249, 1995.
- [3] C. Degen, M. Poggio, H. Mamin, C. Rettner, and D. Rugar. "Nanoscale magnetic resonance imaging." *Proceedings of the National Academy of Sciences*, vol. 106, no. 5, pp. 1313-1317, 2009.
- [4] K. Trepka, R. Hauert, C. Cancellieri, and Y. Tao. "A robust metal oxide thin film with saturation magnetization exceeding 2 Tesla." *Matter*, vol. 3, no. 4, pp. 1263-1274, 2020.
- [5] B. Cockayne, M. Chesswas, and D. Gasson. "Single-crystal growth of sapphire." *Journal of Materials Science*, vol. 2, no. 1, pp. 7-11, 1967.
- [6] N. Ainslie, J. Mackenzie, and D. Turnbull. "Melting kinetics of quartz and cristobalite." *The Journal of Physical Chemistry*, vol. 65, no. 10, pp. 1718-1724, 1961.
- [7] Z. Zhang and M. Lagally. "Atomistic processes in the early stages of thin-film growth." *Science*, vol. 276, no. 5311, pp. 377-383, 1997.
- [8] J. Narayan and B. C. Larson. "Domain epitaxy: A unified paradigm for thin film growth." *Journal of Applied Physics*, vol. 93, no. 1, pp. 278-285, 2003.
- [9] A. Monshi, M. Foroughi, and M. Monshi. "Modified Scherrer equation to estimate more accurately nano-crystallite size using XRD." *World Journal of Nanoscience and Engineering*, vol. 2, no. 3, pp. 154-160, 2012.
- [10] H. Angerer, D. Brunner, F. Freudenberg, O. Ambacher, M. Stutzmann, R. Höppler, T. Metzger, et al. "Determination of the Al mole fraction and the band gap bowing of epitaxial Al_xGa_{1-x}N films." *Applied Physics Letters*, vol. 71, no. 11, pp. 1504-1506, 1997.
- [11] M. Hammar, F. K. LeGoues, J. Tersoff, M. C. Reuter, and R. M. Tromp. "In situ ultrahigh vacuum transmission electron microscopy studies of hetero-epitaxial growth I. Si (001) Ge." *Surface Science*, vol. 349, no. 2, pp. 129-144, 1996.
- [12] T. Metzger, R. Höppler, E. Born, O. Ambacher, M. Stutzmann, R. Stömmer, M. Schuster et al. "Defect structure of epitaxial GaN films determined by transmission electron microscopy and triple-axis X-ray diffractometry." *Philosophical Magazine A*, vol. 77, no. 4, pp. 1013-1025, 1998.
- [13] B. Osgood. "Lecture notes for EE 261: the Fourier transform and its applications." Electrical Engineering Department, Stanford University, 2013.
- [14] W. Huang and D. MacFarlane. "Fast Fourier transform and MATLAB implementation." 2016. Available online at <https://www.utdallas.edu/~dlm/3350%20comm%20sys/FFTandMatLabwanjun%20huang.pdf>.
- [15] M. Ohring. *Materials science of thin films*. Elsevier, 2001.
- [16] R. Davis, G. Kelner, M. Shur, J.W. Palmour, and J.A. Edmond. "Thin film deposition and microelectronic and optoelectronic device fabrication and characterization in monocrystalline alpha and beta silicon carbide." *Proceedings of the IEEE*, vol. 79, no. 5, pp. 677-701, 1991.
- [17] H.J. Jeon, S.C. Yi, and S.G. Oh. "Preparation and antibacterial effects of Ag-SiO₂ thin films by sol-gel method." *Biomaterials*, vol. 24, no. 27, pp. 4921-4928, 2003.
- [18] K. Fichtorn and M. Scheffler. "Island nucleation in thin-film epitaxy: a first-principles investigation." *Physical Review Letters*, vol. 84, no. 23, pp. 5371, 2000.
- [19] S. Emori, D. Yi, S. Crossley, J.J. Wisser, P.P. Balakrishnan, B. Khodadadi, P. Shafer et al. "Ultralow Damping in Nanometer-Thick Epitaxial Spinel Ferrite Thin Films." *Nano Letters*, vol. 18, no. 7, pp. 4273-4278, 2018.
- [20] C. Tellier and A. Tossier. *Size effects in thin films*. Vol. 2. Elsevier, 2016.
- [21] A. Ghorai. "Calculation of Parameter of the Ashcroft Model Potential for Hexagonal Closed Pack (hcp) Crystals." *Acta Physica Polonica*, no. 2, pp. A134, 2018.
- [22] A. Trampert, and K. H. Ploog. "Heteroepitaxy of Large-Misfit Systems: Role of Coincidence Lattice." *Crystal Research and Technology: Journal of Experimental and Industrial Crystallography*, vol. 35, no. 6-7, pp. 793-806, 2000.
- [23] Y. Chen and J. Washburn. "Structural transition in large-lattice-mismatch heteroepitaxy." *Physical Review Letters*, vol. 77, no. 19, pp. 4046, 1996.
- [24] H. Ochoa-Dominguez and K. R. Rao. *Discrete Cosine Transform*. CRC Press, 2019.
- [25] A. Jensen and A. Cour-Harbo. *Ripples in mathematics: the discrete wavelet transform*. Springer Science & Business Media, 2001.
- [26] K. Simonyan and A. Zisserman. "Very deep convolutional networks for large-scale image recognition." *arXiv preprint arXiv:1409.1556*, 2014.
- [27] F. Karimzadeh, A. Ebnonnasir, and A. Foroughi. "Artificial neural network modeling for evaluating of epitaxial growth of Ti6Al4V weldment." *Materials Science and Engineering: A*, vol. 432, no. 1-2, pp. 184-190, 2006.

APPLICATION NOTE

A COMPARATIVE STUDY OF ATOMIC FORCE MICROSCOPY BETWEEN AM-KPFM AND SIDEBAND KPFM, PRINCIPLES AND APPLICATIONS

Research Application Technology Center, Park Systems Corporation

Introduction

Since the development of Atomic Force Microscopy (AFM) [1], several measurement modes have been developed that characterize electrical, mechanical, magnetic, and thermal properties. Among those, Kelvin Probe Force Microscopy (KPFM) [2] is a well-known mode that enables the monitoring of both surface morphology and surface potential distribution properties on a nanometer scale. KPFM has been utilized extensively to investigate the localized charge distributions on a surface layer [3], local surface potential distributions [4] variations of surface work functions [5] and ferroelectric domains [6], in a variety of research fields. KPFM can simultaneously deliver both surface topographical information and surface potential/work functions of the sample by applying AC and DC voltage. Using the same configuration as electrostatic force microscopy (EFM), KPFM monitors the surface potential and work function of samples by applying a DC bias (VDC) to nullify tip-sample potential difference. The VDC to the cantilever is equal to the surface potential (VS). The feedback signal, VDC, then generates the surface potential map. In the conventional method, amplitude modulation (AM)-KPFM, the measurement signal directly relates to the electrostatic force between the sample surface and tip via the amplitude of the AC frequency signal (Figure 1a). This implies that AM-KPFM is mainly affected throughout the AFM cantilever, which has low resolution due to an averaging effect [7] [8].

However, Sideband KPFM has an advantage in terms of the spatial resolution of the surface potential measurement relative to AM-KPFM [9]. When the AC voltage (VAC) is applied between the AFM tip and the sample, an oscillating electrostatic force is generated between the tip and sample. The resonance frequency of the cantilever (f₀) is modulated by the electrostatic force. In the frequency spectrum of the

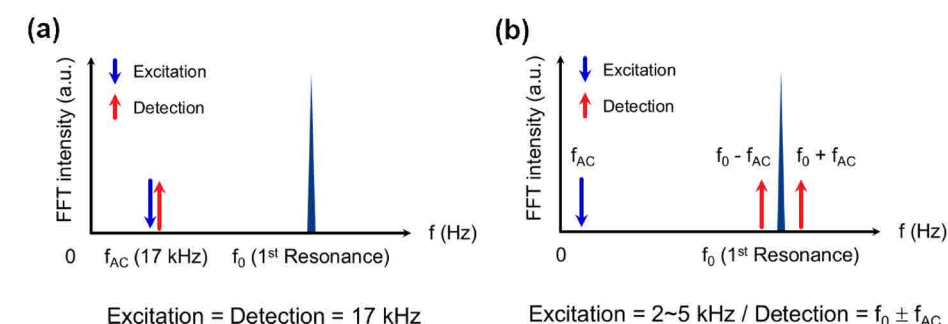


Figure 1. Frequency monitoring on AM-KPFM and Sideband KPFM.

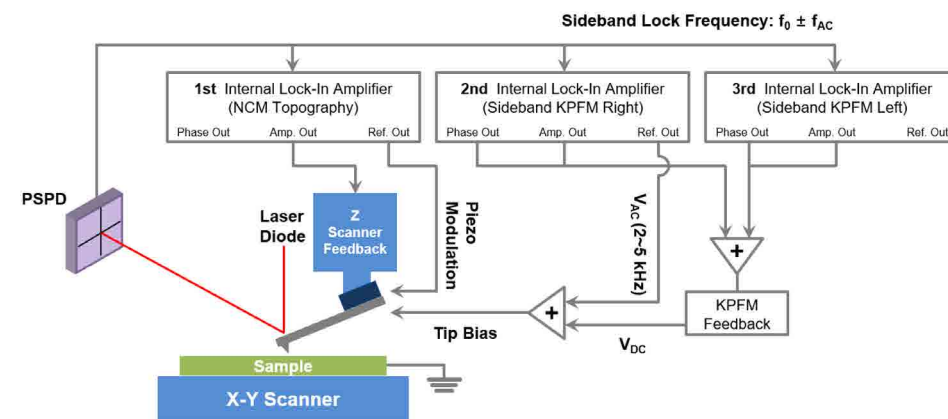


Figure 2. Connection diagram of Sideband KPFM.

cantilever deflection signal, sidebands appear at $f_0 + f_{AC}$ and $f_0 - f_{AC}$ (Figure 1b). Application of a DC voltage, which matches the Fermi level between the AFM tip and the sample, compensates for the electrostatic force, and the sideband disappears. In measuring the DC voltage required to compensate for the electrostatic force, the work function of the sample can be estimated. Unlike AM-KPFM, Sideband KPFM is mainly affected by the AFM tip apex. It detects the electrostatic force gradient by frequency changes and results in better resolution.

In this study, we present results obtained with AM-KPFM and Sideband KPFM on well-defined samples with extended areas of different surface potentials. From these results, we directly compare the spatial resolution of AM-KPFM and Sideband KPFM under identical

conditions. **Materials and Methods**
Sideband KPFM
Sideband KPFM is an optional AFM mode used to measure electrical properties of a sample surface. Figure 2 shows the connection diagram of Sideband KPFM which uses two lock-in amplifiers to measure the amplitude and phase of each sideband. On lock-in amplifiers 2 and 3, a signal with a frequency of $f_0 \pm f_{ac}$ is used as the reference signal (lock-in amplifiers 2) to decouple the sideband signals with a frequency of $f_0 \pm f_{ac}$ in the deflection signal (lock-in amplifiers 2 and 3). The decoupled signals from the two lock-in amplifiers are averaged and used for feedback into DC voltage. The AFM controller applies a corresponding VDC so the averaged sideband peak size becomes zero (As tip bias servo in Park SmartScan™).

Test samples and AFM cantilever

ZYH grade highly-ordered pyrolytic graphite (HOPG, SPI Supplies) was utilized for showing layer by layer surface potential differences. A silicone substrate with low conductivity polymer dots was used to display the surface potential contrast of two different materials. An IFX dopant calibration sample (NP20, Infineon) was chosen to monitor the stepwise electrical signal. This sample consisted of 5 different n-type implant areas in order to compare the electrical signals. All imaging was performed using an Au coated NSC36-C (resonance frequency, 65 kHz; spring constant, 0.6 N/m; length, 130 μm) with the same AFM parameters.

Results and discussion

This study analyzes three different samples to compare the electrical resolution performances of AM-KPFM and Sideband KPFM. Figure 3 shows surface potential images of HOPG by AM-KPFM and Sideband KPFM. Sideband KPFM confirms the sharp contrast due to the HOPG layer, whereas AM-KPFM shows blurry edges. As shown in the line profile analysis, Sideband KPFM has an approximately two-fold higher surface potential difference on layers (~ 70 mV) than AM-KPFM (~ 35 mV, red arrow). Also, Sideband KPFM displays small HOPG fragments very clearly, while AM-KPFM shows a blurry image.

Next, the analysis of polymer dots on a silicone substrate was performed by AM-KPFM and Sideband KPFM. Additionally, Sideband KPFM both in and out of lift mode were compared to investigate the non-contact feedback performance for Sideband KPFM. In Figure 4, all images show contrasts between the polymer dots and the silicone substrate. However, AM-KPFM indicates a lower surface potential contrast than Sideband KPFM including lift mode. For Sideband KPFM, there is no significant difference between the no-lift mode and a 5 nm lift mode, which the line profile analysis confirms. Surface potential differences between the polymer dots and the silicone substrate are approximately 180 mV in AM-KPFM, ~ 300 mV for the no-lift Sideband KPFM, and ~ 330 mV for the 5 nm lift Sideband KPFM.

Lastly, AM-KPFM and Sideband KPFM were used on a IFX dopant calibration sample to compare stepwise electrical resolution. In AM-KPFM, different doping level of n-type implant are recognized; however, checking the electrical signal step was difficult. In contrast, the stepwise electrical signal is displayed in both no-lift

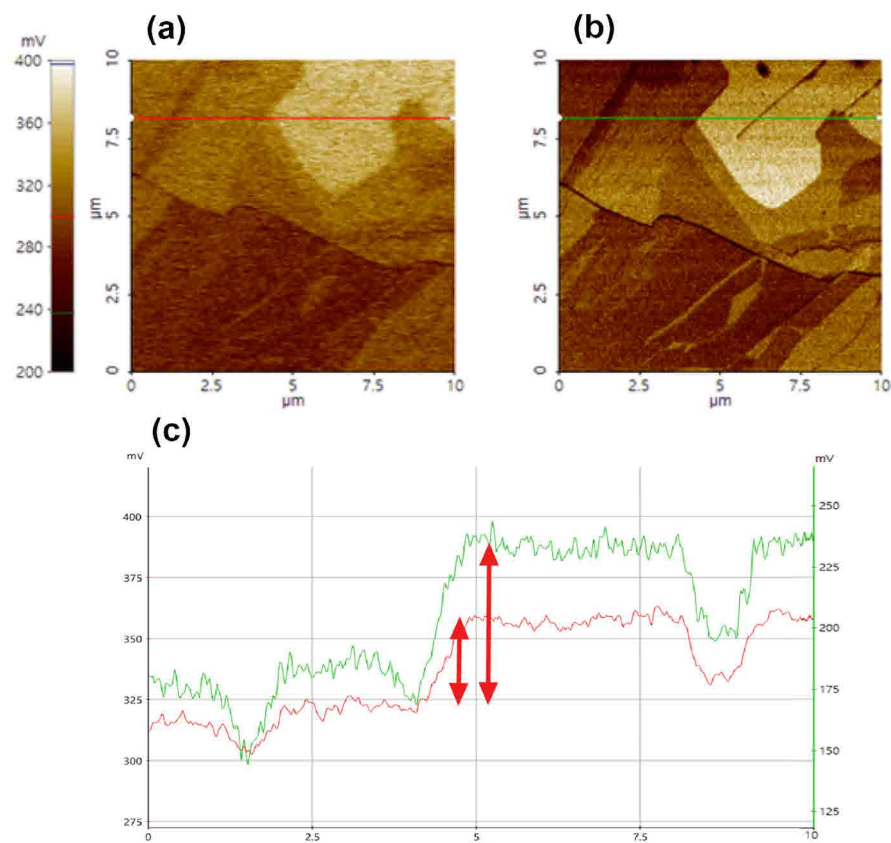


Figure 3. The comparison of surface potential between AM-KPFM (a) and Sideband KPFM (b) on a HOPG sample with a line profile analysis (c).

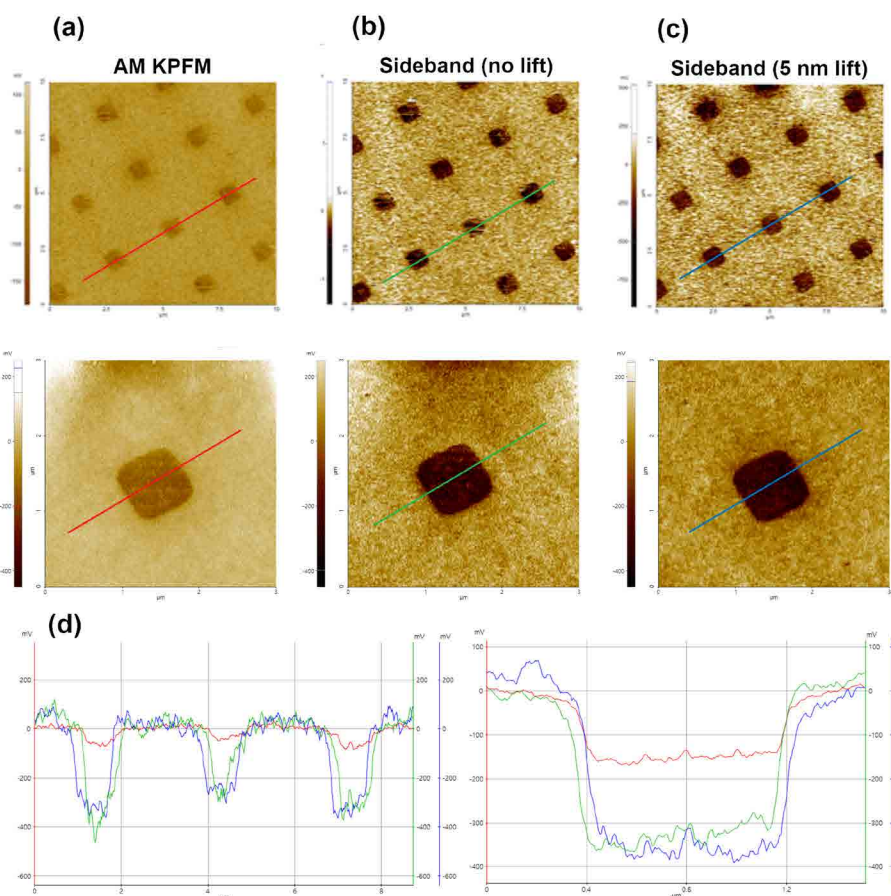


Figure 4. Comparison of surface potential between AM-KPFM (a), Sideband KPFM with no lift (b) and Sideband KPFM with 5 nm lift (c) on polymer dots sample with line profile analysis (d).

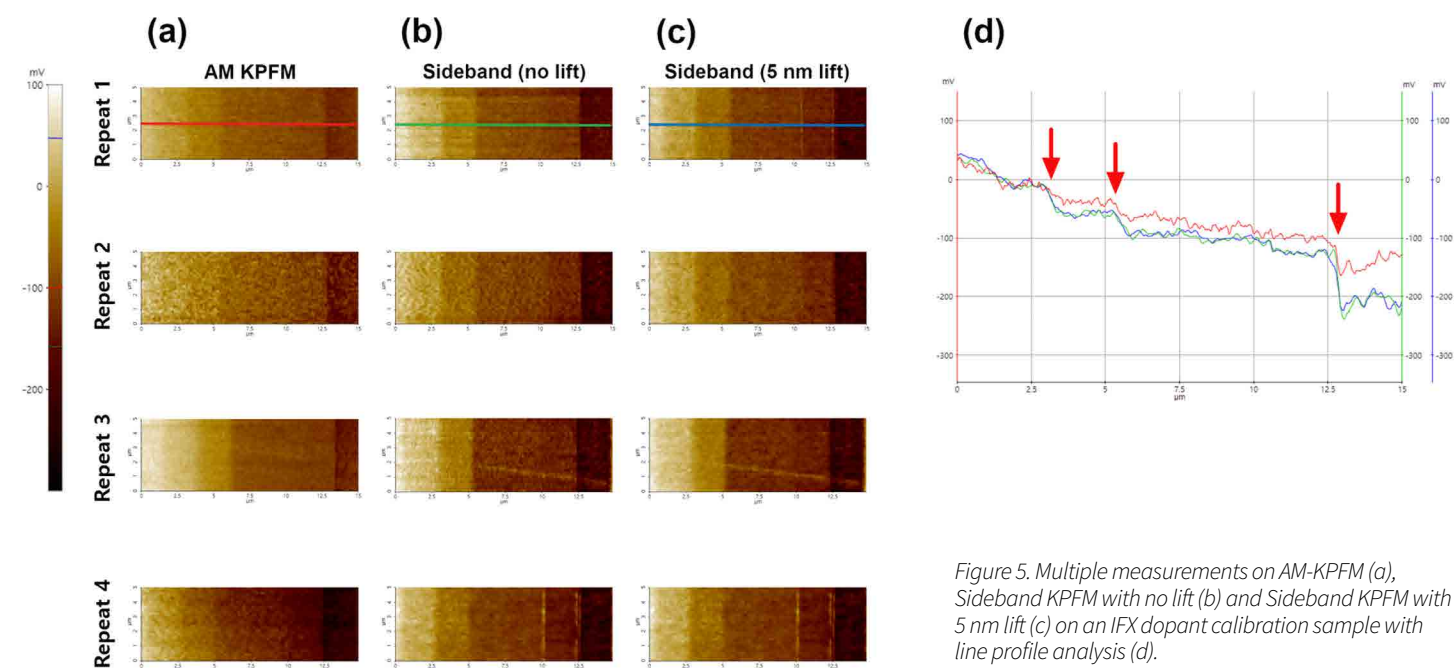


Figure 5. Multiple measurements on AM-KPFM (a), Sideband KPFM with no lift (b) and Sideband KPFM with 5 nm lift (c) on an IFX dopant calibration sample with line profile analysis (d).

and 5 nm lift Sideband KPFM. Based on several repetitive tests, all Sideband KPFM analyses show better resolution than those of AM-KPFM. As the line profile suggests, Sideband KPFM can monitor step-by-step surface potential differences, though AM-KPFM can detect a gradual signal decrease.

Conclusions

In this study, we compare AM-KPFM and Sideband KPFM using a variety of samples. Those results indicate that Sideband KPFM has superior resolution relative to AM-KPFM. In surface potential images, Sideband KPFM shows a clear electrical contrast and detects relatively small changes. From a line profile analysis, the surface potential differences in Sideband KPFM are higher than that of AM-KPFM, which qualifies the superior performance of Sideband KPFM. However, the comparison between no lift and 5 nm lift in Sideband KPFM shows no difference for all tested samples. Due to the accuracy of Park Systems's AFM feedback system, there is no tapping between the AFM tip and sample surface. Thus, it is possible to obtain the

true surface morphology and a clear KPFM signal as well.

Since the development of KPFM, it has become one of the more useful AFM options utilized by surface material science and in semiconductor engineering. It is a unique technique for surface potential or work function mapping on the nanoscale, and the Sideband KPFM option offers superior spatial resolution and improved electrical sensitivity for material characterizations.

References

1. Quate, C. F., Gerber, C., & Binnig, C. (1986). Atomic force microscope. *Phys. Rev. Lett.*, 56(9), 930-933.
2. Nonnenmacher, M., o'Boyle, M. P., & Wickramasinghe, H. K. (1991). Kelvin probe force microscopy. *Applied physics letters*, 58(25), 2921-2923.
3. Lü, J., Delamar, E., Eng, L., Bennewitz, R., Meyer, E., & Güntherodt, H. J. (1999). Kelvin probe force microscopy on surfaces: investigation of the surface potential of self-assembled monolayers on gold. *Langmuir*, 15(23), 8184-8188.
4. Liu, L., & Li, G. (2010). Electrical characterization of single-walled carbon nanotubes in organic solar cells by Kelvin probe force microscopy. *Applied Physics Letters*, 96(8), 33.
5. Bielecki, M., Hynninen, T., Soini, T. M., Pivetta, M., Henry, C. R., Foster, A. S., ... & Heiz, U. (2010). Topography and work function measurements of thin MgO (001) films on Ag (001) by nc-AFM and KPFM. *Physical Chemistry Chemical Physics*, 12(13), 3203-3209.
6. Wu, W., Horibe, Y., Lee, N., Cheong, S. W., & Guest, J. R. (2012). Conduction of topologically protected charged ferroelectric domain walls. *Physical review letters*, 108(7), 077203.
7. Melitz, W., Shen, J., Kummel, A. C., & Lee, S. (2011). Kelvin probe force microscopy and its application. *Surface science reports*, 66(1), 1-27.
8. Garrett, J. L., & Munday, J. N. (2016). Fast, high-resolution surface potential measurements in air with heterodyne Kelvin probe force microscopy. *Nanotechnology*, 27(24), 245705.
9. Stan, G. (2020). High-speed digitization of the amplitude and frequency in open-loop



Park Systems Announces \$1 Million Dollar Nano Research Grant Fund

If you are a researcher at a university or government startup lab you may be eligible for a Park Nano Grant. We started the Park Nano Grant program to support researchers that require atomic force microscopy equipment for their up and coming research.

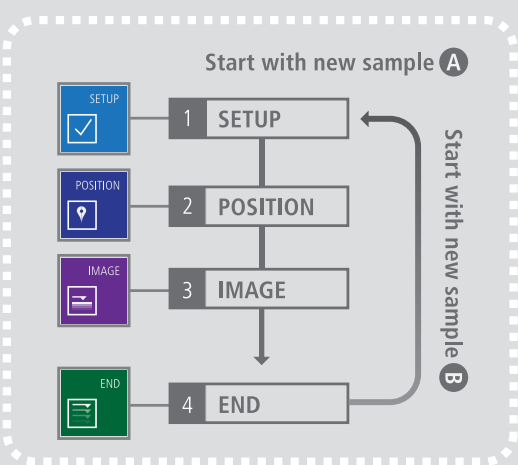
Visit www.parksystems.com/grant to apply and learn more.





Park SmartScan™

Bringing the power and versatility of AFM technology to everyone



Single-Click Imaging with SmartScan Auto Mode

Park SmartScan™ is the revolutionary operation software for Park atomic force microscopes (AFM) that lets inexperienced users scan in Auto Mode with single-click imaging to acquire high quality nanoscale data that rival those obtained manually by experts. Once the user is prepared to image, the user points out a region of interest and a simple click begins the scan. Park SmartScan™ also includes a Manual Mode that provides all the functions, tools, and fine controls seasoned users expect and a Batch Mode for high productivity operation. This combination of extreme versatility, ease-of-use, and quality makes Park AFMs the most powerful atomic force microscopes available.



To learn more about Park SmartScan
Please visit parksystems.com/smartscan or email: inquiry@parksystems.com

Park
SYSTEMS
parksystems.com